Achieving multiple effects of 3D-printed NiTi-based alloys via laser beam manipulation and their mutual collaboration for heat-driven elastocaloric cooling

Xiangbin Xu , Chenglong Ma , Rossitza Setchi , Yu Liu ,
Dongya Li , Guotao Zhang , Quanlong Wang , Meiping Wu

PII: S2950-4317(25)00102-9
DOI: https://doi.org/10.1016/j.amf.2025.200292
Reference: AMF 200292

To appear in: *Additive Manufacturing Frontiers*

Received date: 15 October 2025
Revised date: 23 November 2025
Accepted date: 2 December 2025

Please cite this article as: Xiangbin Xu , Chenglong Ma , Rossitza Setchi , Yu Liu , Dongya Li , Guotao Zhang , Quanlong Wang , Meiping Wu , Achieving multiple effects of 3D-printed NiTi-based alloys via laser beam manipulation and their mutual collaboration for heat-driven elastocaloric cooling, *Additive Manufacturing Frontiers* (2025), doi: https://doi.org/10.1016/j.amf.2025.200292

Achieving multiple effects of 3D-printed NiTi-based alloys via laser beam manipulation and their mutual collaboration for heat-driven elastocaloric cooling

Xiangbin Xu[a], Chenglong Ma[a, b, *], Rossitza Setchi[c], Yu Liu[a, b], Dongya Li[a, b], Guotao Zhang[d], Quanlong Wang[a, b], Meiping Wu[a, b]

[a]Jiangsu Key Laboratory of Advanced Food Manufacturing Equipment & Technology, School of Mechanical Engineering, Jiangnan University, Wuxi, 214122, China

[b] Jiangsu Province Engineering Research Center of Micro-Nano Additive and Subtractive Manufacturing, Wuxi, 214122, China

[c] School of Engineering, Cardiff University, Cardiff , CF24 3AA, UK

[d] China Key System & Integrated Circuit Co., Ltd, Wuxi, 214072, China

*Corresponding author. E-mail: chenglongma@jiangnan.edu.cn (C. Ma)

Abstract

NiTi alloys can be made to demonstrate multiple effects including the shape memory effect (SME), superelastic effect (SE), and elastocaloric effect (eCE), by finely tailoring the Ni content. Notably, laser 3D printing technology has shown great potential for manufacturing NiTi alloys with tunable Ni contents and different phase transformation temperatures (TTs) by changing the laser energy input. Hence, through processing-parameter design, laser 3D-printed NiTi alloys with various functional behaviors can be achieved. This, in turn, potentially enables the rapid prototype manufacturing of a compact multi-effect coupled heat-driven elastocaloric cooling device. However, the mechanisms governing functional differentiation using this technology remain unclear. This study evaluated the integration of laser 3D printing technology and a microstructure-derived functional differentiation strategy to verify the feasibility of heat-driven elastocaloric cooling. By strategically manipulating the laser power (P) and scanning speed (v) across 30 parameter sets, we achieved a precise functional differentiation of NiTi alloys from a single pre-alloyed powder. A comprehensive functional map in the P-v plane was established. It delineates the regions dominated by room-temperature SE/eCE or SME. NiTi alloys processed with a low-energy input excel as superelastic refrigerants, whereas those fabricated with a high-energy input are ideal thermal actuators. Furthermore, the physical mechanisms underlying this tunable functional behavior were revealed through detailed microstructural characterizations. This work has provided a fundamental and practical framework for laser 3D printing of functionally graded NiTi components, thereby paving the way for the development of compact, self-driving, and efficient elastocaloric cooling systems.

Keywords: Laser 3D printing; NiTi alloys; Shape memory effect; Superelastic effect; Elastocaloric effect

1. Introduction

Solid-state refrigeration technology based on the field-induced thermal effect of phase-change materials is becoming a key direction in the current development of refrigeration technology, due to its high efficiency and zero pollution. Owing to its unique advantages such as low cost and wide availability of materials, elastocaloric refrigeration technology has been included successively in the 2017 US Department of Energy report and the UK's technology roadmap for addressing the global carbon reduction challenge in 2050. It is regarded as the most promising new refrigeration technology to replace traditional vapor compression refrigeration (VCR) [1]. Elastocaloric working medium, as the core of elastocaloric refrigeration devices, can undergo reversible martensitic phase transformation and produce significant heat absorption and release effects under the action of a stress field [2]. At present, the most practical materials with the largest reported elastocaloric effect (eCE) are NiTi alloys [3, 4]. A recent study showed that a 0.1 mm NiTi alloy wire can meet the refrigeration requirements of a 0.9 L space at a frequency of 0.152 Hz [1]. Since 2010, many elastocaloric refrigeration prototype devices based on NiTi alloys have been disclosed publicly [1, 5, 6]. However, considering the inherent high phase transformation critical stress of NiTi alloys [7], these elastocaloric refrigeration prototype devices have to rely on complex and cumbersome mechanical drive mechanisms that can result in a driver-to-refrigerant mass ratio of over 500 [8]. This significantly reduces the refrigerating power per unit volume and energy efficiency of the overall elastocaloric refrigeration device.

Notably, NiTi alloys are well known primarily because of their unique thermally driven shape memory effect (SME) and stress-induced superelastic effect (SE), rather than the eCE. SME-dominated NiTi alloys can be developed as a type of thermally actuated device for intelligent control. This device has a compatible bearing and driving capacity, high energy density (over 10 J/cm^3, 25 times higher than that of traditional motors), and environmental sensing capabilities [9], and can perfectly match the driving characteristics (a large driving force and small stroke) required by elastocaloric refrigeration devices [10]. On this basis, the concept of a heat-driven elastocaloric cooling system has been proposed [8, 11]. In principle, this new concept can achieve a driver-to-refrigerant mass ratio with a magnitude of one, thereby solving the aforementioned bottleneck problems. Nevertheless, they studied only the transient characteristics of the new cycle and the utilization of a low-grade heat source using numerical simulation methods. Little attention has been paid to the manufacturing of NiTi alloys with various functional behaviors.

In fact, the functional behavior of NiTi alloys is very sensitive to the Ni content [12]. By precisely regulating the Ni content, NiTi alloys with programmed phase transformation temperatures (TTs) and functional characteristics can be obtained. In recent years, with the rapid development of laser-based additive manufacturing (LAM) technologies, the interest in LAM and the 4D printing of NiTi alloys has increased [13, 14]. According to many previous studies [13-17], owing to the considerable difference in the boiling points of Ni and Ti, LAM can easily achieve controllable adjustments of the input energy and attendant Ni content of as-fabricated NiTi alloys through tailoring of the process parameters (e.g., laser power P, scanning speed v, and hatch spacing h). Hence, by an appropriate process parameter design, an integrated structure containing a NiTi-based SE refrigerator and a NiTi-based SME actuator can be fabricated, thus providing the possibility for the development of compact multifunctional coupled elastocaloric refrigeration devices that integrate self-driving and cooling.

Currently, a growing number of studies are focusing on the eCE and two-way shape memory effect (TWSME) of laser additive-manufactured NiTi alloys [9, 18-20]. Cao et al. studied the effect of post-heat treatment on the elastocaloric properties of NiTi alloys fabricated by laser powder bed fusion (LPBF) [21]. They found that the aged alloy exhibited the largest eCE with an adiabatic temperature change (ΔT_{ad}) as high as 23.2 K. Due to the high yield strength and low stress hysteresis of the aged alloy, this large eCE showed good stability during cycling. Zhan et al. studied the fine-tuning mechanism of the elastocaloric properties of LPBF-fabricated NiTi alloys based on four process parameter combinations (high P and high v, high P and low v, low P and high v, and low P and low v) [22]. They pointed out that although adjusting the Ni loss via laser heat input could effectively control the TTs, inappropriate combinations of laser parameters might result in a lower-than-anticipated cooling capacity. Lu et al. reported an LPBF-fabricated near-equiatomic NiTi alloy with heterogeneous microstructures that achieved a two-way shape memory strain of 0.8% by a cyclic loading–unloading–heating–cooling training process [23]. However, systematic studies on the functional evolution in a wide range of process parameters are lacking, and the underlying microstructure-derived functional differentiation mechanisms remain understudied.

Normally, NiTi alloys fabricated at a low-energy-density input (e.g., low P and high v) tend to exhibit SE at room temperature (RT), whereas those fabricated at a high-energy-density input (e.g., high P and low v) tend to exhibit SME at RT, as shown in Fig. 1. However, the quantitative correlation between laser process parameters and functional characteristics remains unclear. In addition, for LPBF-fabricated NiTi alloys, the influence of the RT SE (or SME) tendency on the elastocaloric performance (or the two-way shape memory strain) remains unclear. Therefore, in this study, we conducted a systematic investigation of the effects of laser processing parameters on the phase transformation behavior (e.g., TTs and enthalpy change) and functional properties (including SE, eCE, and SME) of NiTi alloys fabricated via LPBF using 30 combinations of P and v. A functional differentiation diagram was constructed in the P-v plane. Subsequently, the solidified microstructural features corresponding to different functional regions were characterized to reveal the underlying physical mechanism of the tunable functional behavior induced by the laser processing parameters.

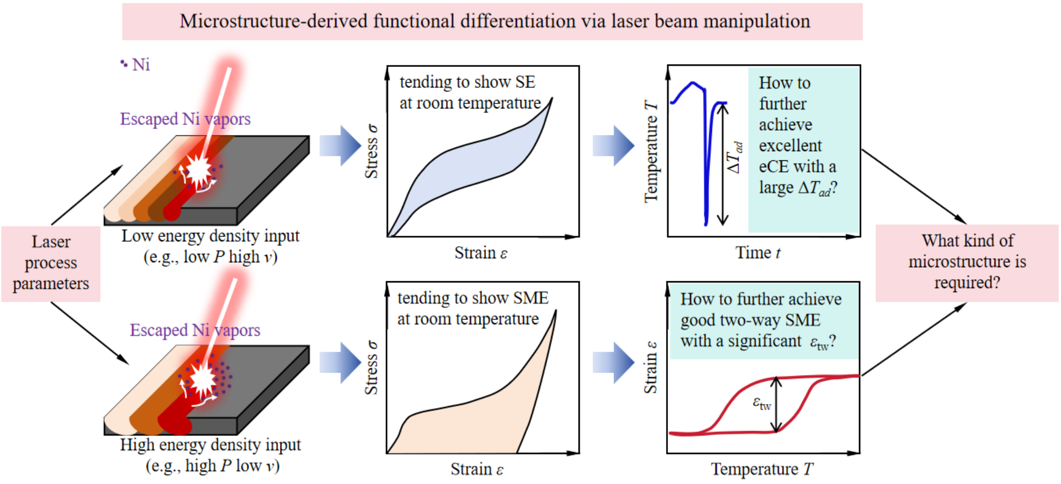

Fig. 1 Critical problem of functional differentiation via laser beam manipulation in the LAM process of NiTi alloys.

2. Experimental Procedure and Methods

2.1 Raw material and LPBF fabrication

In this study, a nearly spherical $Ni_{51.8}Ti_{48.2}$ pre-alloyed powder prepared through electrode induction melting gas atomization (EIGA) by Minatech Co., Ltd. (Shenzhen, China) was used as the raw material. The particle size range of $Ni_{51.8}Ti_{48.2}$ pre-alloyed powder is from 15 to 53 μm, and d_{50} is 37.30 μm. Table 1 lists the detailed chemical composition of the as-used NiTi powder. It demonstrates that the content of impurity elements such as C and O was limited effectively. The particle morphology of the NiTi powder is shown in Fig. 2(a). Most of the NiTi particles presented a relatively high degree of sphericity and smooth surfaces, thereby indicating good powder fluidity, which is important for the powder spreading process. The phase composition and TTs of the NiTi powder were characterized using X-ray diffraction (XRD) and differential scanning calorimetry (DSC), respectively, as shown in Figs. 2(b) and 2(c). It is clearly seen that the B2 austenite phase dominated the NiTi powder at room temperature without any obvious secondary phases detected by XRD. The DSC results also show that the austenitic transformation finish temperature A_f is about 25 °C, which means that the stable phase in raw powder at RT is the B2 austenite phase.

Table 1. The detailed chemical compositions of the as-used NiTi powder prepared by EIGA.

Specimen	Ni (wt%)	Ni (at%)	Ti (wt%)	Fe (wt%)	C (wt%)	O (wt%)	N (wt%)
Powder	56.88	51.8	Bal.	0.011	0.003	0.051	0.003

Subsequently, the NiTi powder was consolidated using an iSLM160 machine (Suzhou ZRapid Technologies Co., Ltd.) equipped with a 500 W IPG ytterbium fiber laser, an automatic powder-spreading device with a flexible scraper blade, and an inert argon gas circulatory protection system. The oxygen concentration in the forming environment was maintained below 100 ppm to minimize the adverse effects of oxygen on the forming quality and functionalities. In addition, the substrate was preheated to 473 K to reduce the temperature gradient and address the high thermal stress. A batch of small bulk specimens with dimensions of 4 mm× 4 mm× 8 mm and thin-walled specimens with dimensions of 1 mm× 5 mm× 5 mm were fabricated (Fig. 2(d)) by using the following processing parameters: laser power *P* of 100–150 W with increments of 10 W, scanning speed *v* of 400–1200 mm/s with increments of 200 mm/s, hatch spacing *h* of 50 μm, and layer thickness *d* of 30 μm. The number of specimens fabricated with different processing parameters is listed in Supplementary material Table S1. A line-scanning strategy with a 90° rotation angle between adjacent layers was applied. Fig. 2(e) shows the relative density distribution map of all the bulk specimens fabricated at different *P* and *v*. The corresponding cross-sectional optical images of the unetched specimens are shown in Supplementary material Fig. S1. It is evident that most of these specimens exhibited a high relative density (⩾ 99.0%), and more than half of these had a relative density of ⩾ 99.5%. Two typical regions with a relatively low degree (Fig. 2(e)) and remarkable metallurgical pores existed (Fig. S1), corresponding to one with a high *P* and low *v* (i.e., *P* = 150 W and *v* = 400 mm/s, featuring spherical pores) and the other with a low *P* and high *v* (i.e., *P* = 120 W and *v* = 1000 mm/s, featuring irregular pores resulting from insufficient fusion). Fig. 2(f) shows the three-dimensional optical images of three typical specimens with different laser energy densities (*VED* = 67 J/mm^3, 133 J/mm^3, and 167 J/mm^3). Although all of them were determined to be nearly dense using the Archimedes method, a few small spherical pores were captured in the P10V10 and P10V4 specimens. This might be attributed to unescaped gas pores and considerable Ni evaporation, respectively. Figs. 2(g) and 2(h) show the LPBF forming process and macro-images of the as-fabricated NiTi-based double helix structure specimens that were used for the multi-effect coupling test in this work.

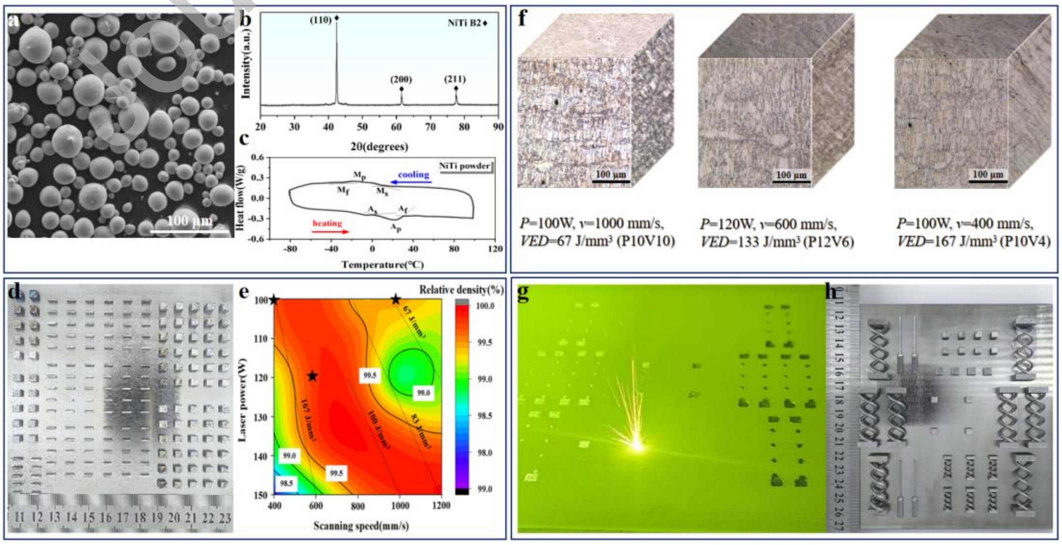

P=100W, *v*=1000 mm/s, *VED*=67 J/mm³ (P10V10)
P=120W, *v*=600 mm/s, *VED*=133 J/mm³ (P12V6)
P=100W, *v*=400 mm/s, *VED*=167 J/mm³ (P10V4)

Fig. 2. Raw powder material and LPBF process: **(a)** SEM image of NiTi powder; **(b)** XRD spectra of NiTi powder within 20°–90° range; **(c)** DSC curve of NiTi powder; **(d)** As-built NiTi bulk specimens; **(e)** Relative density distribution map in *P*-*v* plane; **(f)** Three-

dimensional OM images of three selected specimens corresponding to the black stars in **(e)** (here, $VED = P / (vhd)$); **(g)** Interaction between laser beam and powder bed; **(h)** As-built NiTi double helix structures.

2.2 Characterizations of microstructure and phase transformation behavior

A HITACHI SU1510 scanning electron microscope (SEM, HITACHI High-Tech, Japan) was used to observe the particle morphology of the raw NiTi powder. The as-fabricated bulk specimens were first polished according to a standard metallographic treatment procedure and observed under an optical microscope (OM, DM-2700M, Germany) to characterize the defect distribution. Three typical specimens (P10V10, P12V6, and P10V4) were chosen for the following detailed microscale characterizations: electron backscatter diffraction (EBSD) performed using an FEI Quanta 650 FEG FESEM (FEI. Co., the USA) equipped with an HKL channel 5 system at a voltage of 20 keV for grain orientation and grain size analyses; X-ray diffraction (XRD) detected by the D2 PHASER A26-X1-A2E0B2A0 X-ray diffractometer (Bruker AXS Co., Germany) with Cu K radiation ($\lambda = 0.15418$ nm) using a scan angel range of 20°–90°, a scan speed of 4°/min, and a scan step of 0.01° for phase composition analysis; and transmission electron microscope (TEM) observation via a Tecnai G2 F20 S-TWIN (FEI. Co., USA) operating at 200 kV for the dislocation structures and nanoprecipitates. The thin-walled specimens were used for the DSC tests via differential scanning calorimetry (DSC-TA Q200, the USA) performed in an inert nitrogen stream with a heating/cooling rate of 10 K/min from 193 K to 373 K and a holding time of 1 min at 193 K and 373 K. The TTs including M_f, M_s, A_s, and A_f and the phase transformation latent values $\Delta H^{A\text{-}M}$ and $\Delta H^{M\text{-}A}$ could be determined by the tangent method and integral method, respectively. Each reported DSC datum represents the average of at least three independent measurements.

2.3 Characterizations of functional behavior

The functional behavior was tested using an MTS E45.105 computer-controlled electronic universal testing machine (MTS Industrial Systems (China) Co., Ltd., China). First, the superelastic recoverable behavior was assessed in a quasi-static state where a relatively low constant compressive loading/unloading rate of 10^{-3} s^{-1} was set. Subsequently, based on the superelastic deformation features and previous DSC results, two groups of as-built specimens were selected to characterize the eCE and the two-way shape memory effect (TWSME). Before the eCE test, the specimens first underwent 10 compressive loading–unloading cycles at a maximum stress of 800 MPa to achieve cyclic stabilization. During the eCE testing, a strain rate of 10^{-3} s^{-1} was set for the loading period to ensure isothermal conditions, whereas a higher strain rate of 10^{-1} s^{-1} was applied for the unloading period to achieve adiabatic conditions. Concurrently, the temperature variations in the specimens were monitored using an iRay M200F infrared thermal imager and an SH700-0.1 multi-channel data recorder. For TWSME testing, the specimens were first subjected to a cyclic loading–unloading–heating–cooling training process. During this process, the specimens were loaded to 800 MPa at RT (25 ℃) and then unloaded. After unloading, the specimens were heated above A_f and held for 5 min to complete austenitic transformation. The strain recoverable during the heating process corresponded to a one-way shape memory strain (ε_{ow}). The samples were then cooled in ice water for 5 min to ensure full martensitic transformation. This loading–unloading–heating–cooling cycle was repeated 10 times to activate a stable TWSME. Afterwards, the trained specimens were subjected to thermomechanical analysis (TMA) via Discovery TMA-450 (TransAlta Co., the USA) in compression mode with strict parallelism maintained between the specimen's ends, to evaluate the corresponding two-way shape memory strain (ε_{tw}). The TMA protocol can be described as follows: 1) cooling from RT to -20 °C, 2) holding for 1 min, 3) heating to 120 °C at 5 °C/min, 4) holding for 1 min, and finally 5) cooling to -20 °C at 5 °C/min to complete one thermal cycle. Each reported mechanical property value or measured temperature datum is the average of at least three independent measurements.

3. Results

3.1 Phase transformation behavior

Fig. 3 shows the DSC curves and TT evolution of all the LPBF-fabricated NiTi alloy specimens. Overall, most of the as-fabricated specimens demonstrated a typical single phase transformation path, namely, B19'→B2 for the heating process and B2→B19' for the cooling process. However, at a relatively low *v* like 400 mm/s and even 600 mm/s, an extra small peak was observed in the heating curve corresponding to the reverse transformation process, thereby indicating the occurrence of the B19'→R→B2 multiple-stage transformation [24]. However, during forward transformation, no apparent second peak was observed. This may have been due to the overlap of the two potential peaks. Previous studies have proposed two possible formation mechanisms for the R phase: a misfit elastic thermal stress arising around Ni-rich precipitates and an increased dislocation density [25]. A low *v* indicates a deeper molten pool and higher melting temperature, which increases stress accumulation and the attendant high dislocation density during the solidification process [26]. These dislocations may act as nucleation sites to promote the R transformation. As for the TTs, it was evident see that at a fixed *P* (e.g., *P* = 100 W), an increase in *v* always led to a continuous left shift of TTs (Figs. 3(a)-(f)). In particular, the change in TTs was higher in the range of *v* = 400–800 mm/s. For example, the A_f value decreased sharply from 87.5 ℃ to 49.2 ℃ with *v* increasing from 400 mm/s to 800 mm/s, whereas it showed only a small fall (~11.5 ℃) when *v* was elevated further from 800 mm/s to 1200 mm/s (Fig. 3(a)). This trend is consistent with those reported in other studies [17]. However, at a fixed *v*, the TTs did not follow a monotonic change and rather fluctuated with the increase in *P*. Fig. 3(g) shows the detailed values of M_s for different processing parameters. It was evident that the TTs were more sensitive to the applied *v* rather than *P*. Additionally, M_s lower than RT mainly emerged at a higher *v* like 1000 or 1200 mm/s. This indicates that the RT-solidified microstructure is dominated by the B2 phase under these conditions. Fig. 3(h) displays a heat map of the temperature intervals (M_s-M_f) for martensite transformation in the P-v plane. Most of these specimens showed a larger temperature interval of more than 40 ℃, which usually indicates the existence of remarkably heterogeneous microstructure in the LPBF-fabricated specimens [13]. As the applied P was increased to 140 W, the temperature interval showed an apparent reduction, thereby indicating the positive role of the high-energy input in improving the microstructural homogeneity. Fig. 3(i) further summarizes the evolution of the TTs with the volume energy density (VED). When the applied VED was in the range of 55.6 J/mm^3–133.3 J/mm^3, all the TTs basically exhibited a monotonic rise trend. As the VED was extended further to 166.7 J/mm^3, A_f and M_s showed a slight declining trend, whereas A_s and M_f continued to increase. Meanwhile, at VED = 166.7 J/mm^3, A_f and M_s increased suddenly. When VED was increased further, all the TTs generally displayed a slow downtrend, which might be attributed to the occurrence of severe oxidation.

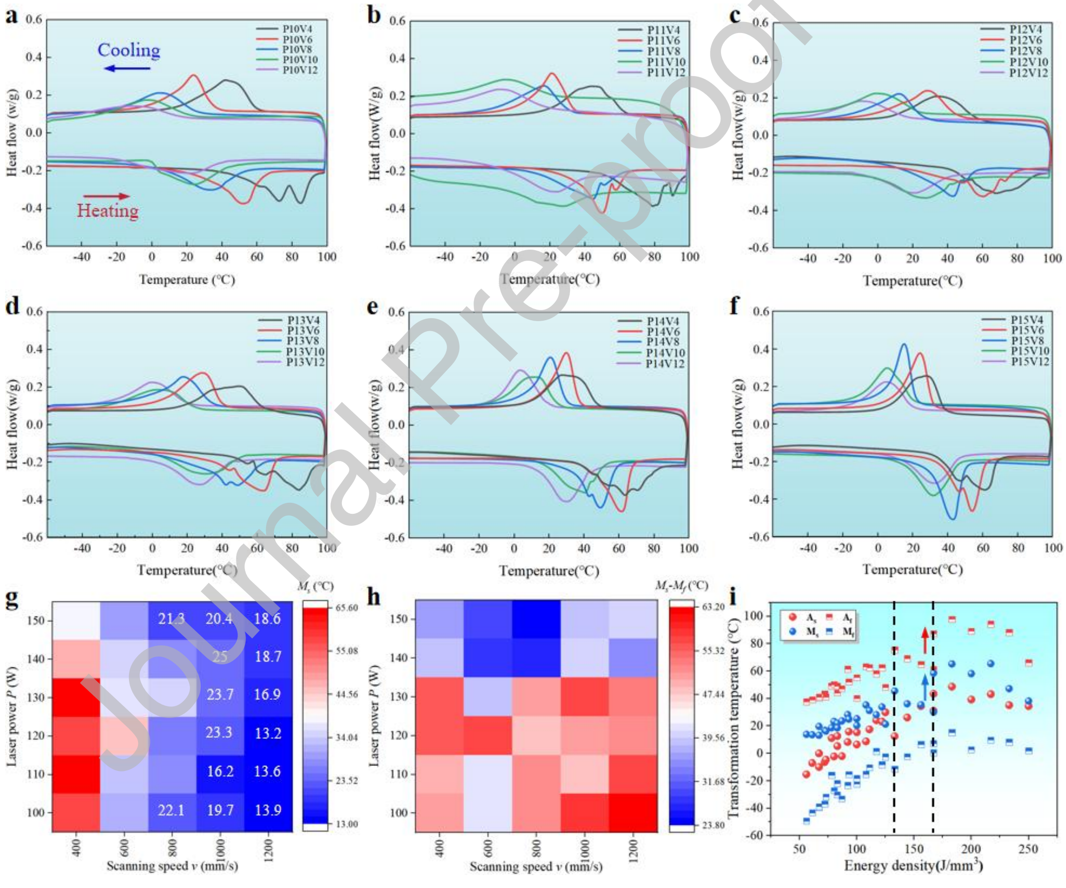

Fig. 3 DSC curves and evolution features of TTs with the variation in laser processing parameters: **(a-f)** DSC curves; **(g)** and **(h)** Heat maps of M_s and the temperature interval M_s-M_f in the P-v plane, where the temperature values lower than RT are marked in **g**; **(i)** Evolution of TTs with the applied VED.

The latent heat (ΔH) of phase transformation corresponding to the peak area is another key indicator. Considering that the phase transformation behavior is more sensitive to the applied v, a new parameter combination, v / VED, was proposed. Fig. 4(a) presents the evolution of the transformation enthalpies ($\Delta H^{A\to M}$, $\Delta H^{M\to A}$) with v / VED. Both the transformation enthalpies exhibited an approximately linear decline with the applied v / VED. This suggests that a lower *VED* with a smaller *v* is conducive to enhancing latent heat, which is consistent with the findings of Zhan et al. [22]. In particular, the reverse transformation enthalpy change $\Delta H^{M\to A}$ can be used to calculate the reverse transformation entropy change $\Delta S^{M\text{-}A}$ via $\Delta S^{M\text{-}A} = \Delta H^{M\to A} / T_{eq}$, where T_{eq} is the equilibrium temperature and is expressed as $(A_f + M_s) / 2$ [27]. Fig. 4(b) shows the scatter plots of T_{eq} and $\Delta S^{M\text{-}A}$ as functions of *v* / *VED*. It is seen that both T_{eq} and $\Delta S^{M\text{-}A}$ roughly presented a gradually decreasing trend with the increase in *v* / *VED*, except for several abnormal data for $\Delta S^{M\text{-}A}$ (marked by the black dotted circle). Normally, a higher $\Delta S^{M\text{-}A}$ value is more favorable for achieving a superior eCE with a larger ΔT_{ad} [22]. Hence, to obtain a significant $\Delta S^{M\text{-}A}$, the process parameter combination of *v* / *VED* should be minimized. However, this also leads to a higher T_{eq} value, which does not effectively meet the demand for the room-temperature refrigeration.

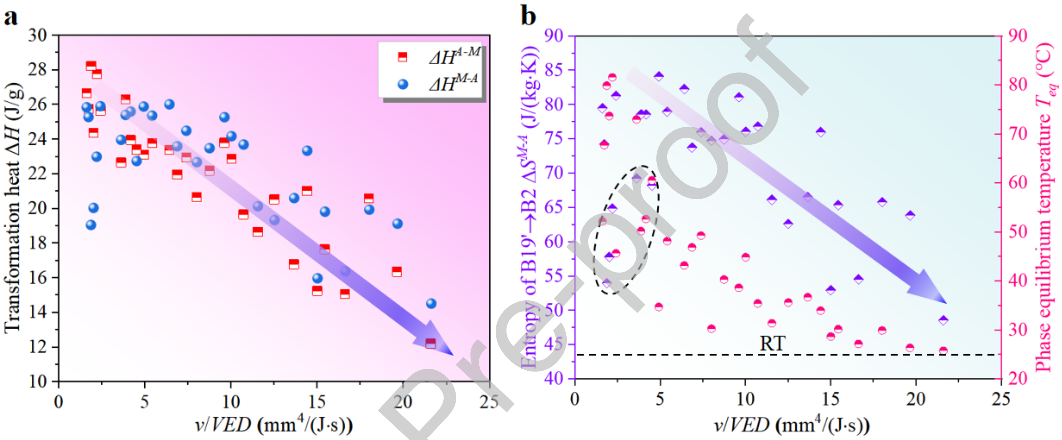

Fig. 4 **(a)** Evolution of ΔH with *v* / *VED*; **(b)** evolution of T_{eq} and ΔS with *v* / *VED*.

3.2 Mechanical response

Subsequently, we evaluated the mechanical response behavior of all the LPBF-fabricated NiTi specimens via a single loading–unloading compressive cycle test at RT, as shown in Fig. 5. Three main indicators were considered: the plateau critical stress σ_c, recoverable strain ε_{rec}, and recoverable strain ratio ξ (defined as the ratio of ε_{rec} to the applied strain ε_{app}). σ_c was obtained using the tangent offset method. At a fixed *P* such as 100 W, an increase in *v* tended to cause a synergistic rise in σ_c and ε_{rec} (Fig. 5(a)). For example, with *v* increasing from 400 mm/s to 1200 mm/s (*P* = 100 W), σ_c and ε_{rec} increased by 369.47% and 54.75%, respectively. The variations in these critical indicators, to some degree, demonstrated a switch from SME-dominated to SE-dominated behavior. Specifically, as *P* increased, the specimens were more inclined to exhibit an RT SME than an SE (Figs. 5(a)-(f)). Meanwhile, at higher *P* values such as 140 W or 150 W, *v* played a limited role in tailoring σ_c and ε_{rec}.

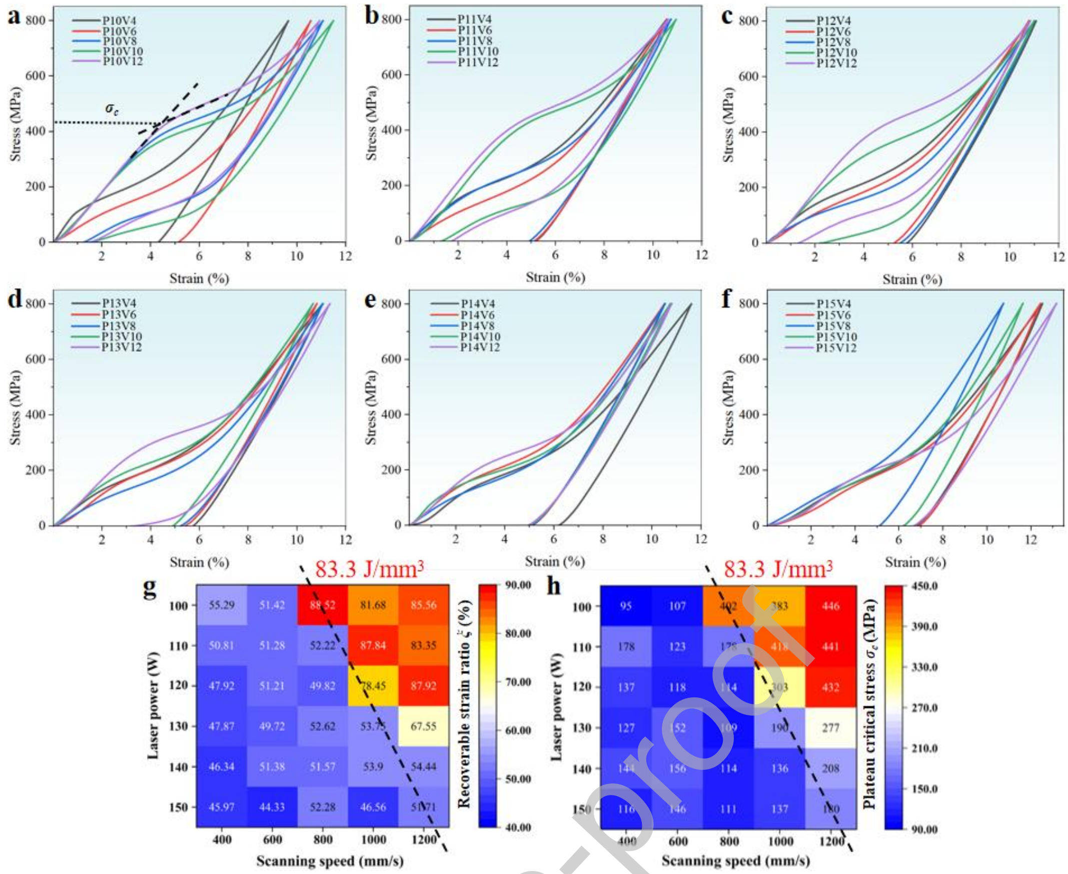

Fig. 5. RT compressive response behavior for a single loading–unloading cycle: **(a-f)** RT loading–unloading compressive stress–strain curves of all the LPBF-fabricated specimens; **(g, h)** heat maps of ξ and σ_c in the P-v plane.

To better manifest the influence of the laser processing parameter on the mechanical response, the detailed σ_c and ξ values were listed in the form of a heat map, as shown in Figs. 5(g) and 5(h). A completely overlapping delta region for σ_c and ξ was evident. These were roughly partitioned by a *VED* of 83.3 J/mm^3, which corresponds to the bright warm color region (including P10V8, P10V10, P10V12, P11V10, P11V12, P12V10, P12V12, and P13V12). The σ_{tr} and ξ values in the warm color region were signally higher than those in the cool color region (exceeding at least 33.17% and 22.17%, respectively). Hence, it can be deduced that a combination of a low P and high v is conducive to a good superelastic response.

Considering that the selective sensitivity of σ_c and ξ to P or v is negligible, we further associated σ_c and ξ with the laser energy density *VED*, as shown in Fig. 6(a). At a lower *VED* (e.g., 66.7 J/mm^3), both σ_c and ξ showed a higher value, reaching 400–450 MPa and 80–90%, respectively. Subsequently, a sudden and rapid drop occurred as the applied *VED* reached ~83.3 J/mm^3. When the applied *VED* was higher than 83.3 J/mm^3, both σ_c and ξ values declined rapidly to low levels (corresponding to ~150 MPa and ~50%, respectively). Moreover, at a higher *VED* of 166.7 J/mm^3, a small peak also existed. Specially, the evolution trends of σ_c and ξ with the applied *VED* were highly consistent. By a linear fit, the relationship between σ_c and ξ can be described roughly by the equation $\xi = 0.12\sigma_c + 34.16$, with a relatively high R^2 of 0.91. This suggests that the LPBF-fabricated NiTi-based specimens with a large

σ_c tended to present good superelastic performance, while those with a low σ_c were more likely to achieve a considerable shape memory strain by thermal stimulus. Notably, according to Fig. 6(a), a good superelastic performance is obtained mainly at a low *VED*, such as a combination of low P and high v. However, as shown in Fig. 4(b), a remarkable eCE tends to be achieved at a high *VED* in an appropriate operating temperature range, which seems to show a tradeoff with SE enhancement. However, for the RT operation, the measured ΔT_{ad} cannot be related directly with $\Delta S^{M\text{-}A}$. From the perspective of energy conversion, L. Ding et al. [28] pointed out that ΔT_{ad} is positively associated with the mechanical work released by the reverse transformation during unloading. Fig. 6(c) shows the relationship between the released mechanical energy E_{rel} and *VED*. Interestingly, E_{rel} exhibited a similar evolution rule as σ_c or ξ with the increase in *VED*. Therefore, E_{rel} is proportional to σ_c or ξ. Fig. 6(d) shows the relationship between E_{rel} and ξ with a fitted equation of $E_{rel} = 0.157\xi + 11.853$. This indicates that a good SE is conducive to the attainment of considerable RT eCE.

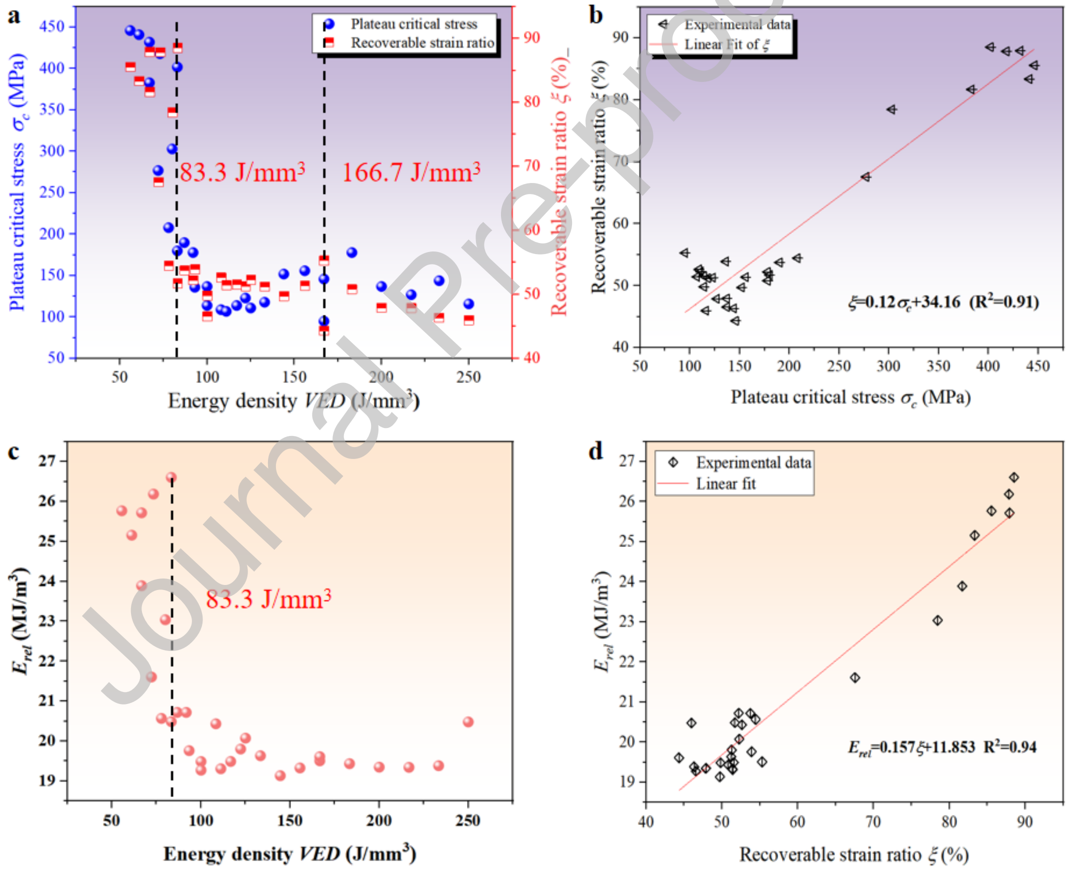

Fig. 6 Relationship between σ_c, ξ, E_{rel}, and *VED*: **(a)** Evolution of ξ and σ_c with the applied *VED*; **(b)** Fitted linear relationship between σ_c and ξ; **(c)** Evolution of E_{rel} with the applied *VED*; **(d)** Fitted linear relationship between E_{rel} and ξ.

3.3 Superelasticity and elastocaloric effect

Based on the RT mechanical responses described in Section 3.2, it is believed that a combination of low P and high v or a relatively low *VED* can achieve better superelasticity and potentially large RT eCE. Therefore, we further conducted the cyclic loading–unloading tests and corresponding ΔT_{ad} measures for the specimens marked as P10V8,

P10V10, P10V12, P11V10, P11V12, P12V10, P12V12, and P13V12. Fig. 7 shows the cyclic compressive stress–strain curves, as well as the variations in irrecoverable strain ε_{ir} with the cycle number. Among these specimens, those with high P (e.g., 120 W or 130 W) had a significant ε_{ir} (more than 2%) in the initial cycle, while the other ones with low P exhibited a relatively small ε_{ir} value. As the cyclic number increased, ε_{ir} decreased rapidly. After 10 cycles, excellent superelasticity with significantly reduced hysteresis area was observed for all the selected specimens. Table 2 summarizes the irrecoverable (ε_{ir}), recoverable (ε_{rec}), and total (ε_{tot}) strains, as well as the stored energy ratio ΔE / E_{tot} for the first and last cycles. Here, ΔE is the hysteresis loop area between the loading and unloading curves (as the energy dissipation), and E_{tot} is the area under the loading curve. The results show that the P10V8 specimen exhibited the lowest accumulated ε_{ir} (3.93%) and highest stabilized ε_{rec} (8.34%) after 10 cycles. The poorest superelastic response was obtained for the P12V10 specimen, which showed only a 6.40% strain recovery in the 10th cycle and a 71.52% recoverable strain ratio in the 1st cycle. The E_{rel} values for the last cycle are listed in Table 2. It was found that the evolution of E_{rel} with the process parameters was highly similar to that of the stabilized ε_{rec} and ΔE / E_{tot}. As shown in Table 2, the P10V8 specimen had the largest E_{rel} (25.63 MJ/m^3), while the P12V10 specimen demonstrated the lowest E_{rel} (reduced by 15%). In view of the positive correlation between E_{rel} and ΔT_{ad}, it can be deduced that the largest and smallest ΔT_{ad} values were more likely to be achieved in the P10V8 and P12V10 specimens, respectively.

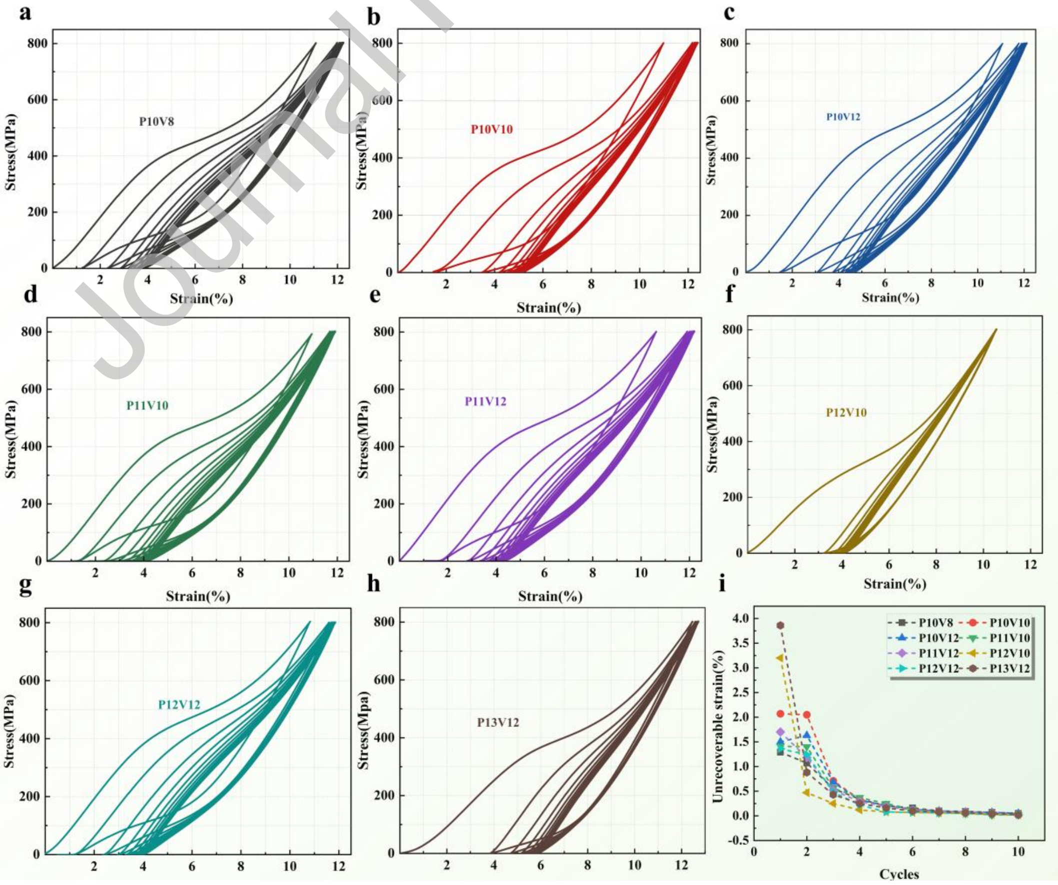

Fig. 7 Cyclic loading–unloading behavior: **(a-h)** Cyclic compressive stress–strain curves of the selected 8 typical specimens; **(i)** evolution of ε_{ir} with the cycle number.

Table 2. The measured ε_{tot}, ε_{rec}, ξ, and $\Delta E/E_{tot}$ for 1st cycle and total ε_{ir}, stabilized ε_{rec}, $\Delta E/E_{tot}$ and E_{rel} for 10th cycle.

Specimens	$\sigma_{\max}$ (MPa)	1st Cycle				10th Cycle			
		ε_{tot} (%)	ε_{rec} (%)	ξ (%)	$\Delta E/E_{tot}$	*Total* ε_{ir} (%)	*Stabilized* ε_{rec} (%)	$\Delta E/E_{tot}$	E_{rel} (MJ/m^3)
P10V8	800	11.07	9.78	88.35	0.41	3.93	8.34	0.21	25.63
P10V10	800	11.02	9.43	85.57	0.46	5.05	7.24	0.16	23.04
P10V12	800	11.08	9.57	86.37	0.45	4.72	7.44	0.17	23.98
P11V10	800	10.94	9.53	79.82	0.42	4.24	7.76	0.21	23.07
P11V12	800	10.63	8.92	83.91	0.45	4.58	7.75	0.19	24.20
P12V10	800	11.20	8.01	71.52	0.42	4.78	6.40	0.11	21.79
P12V12	800	10.83	9.48	87.53	0.43	4.93	7.80	0.20	24.40
P13V12	800	12.46	8.59	68.17	0.51	5.94	6.83	0.17	21.76

Subsequently, the above specimens were further tested via a slowly loading ($\mathrm{d}\varepsilon/\mathrm{d}t = 0.001$/s) and rapidly unloading ($\mathrm{d}\varepsilon/\mathrm{d}t = 0.1$/s) method to evaluate the refrigeration performance at RT, as shown in Fig. 8. Fig. 8(a) shows the infrared temperature contour images of the P10V8 specimen at different stages of the loading–unloading test. A significant temperature decrease was observed when the specimen was unloaded rapidly. Figs. 8(b) and 8(c) show the compressive loading–unloading curves and corresponding temperature change curves, respectively. Owing to the application of a significantly higher strain rate during the unloading process, the loading and unloading curves intersected. However, these trained specimens failed to demonstrate perfect superelasticity at such high strain rates. As for the measured temperature change, the P10V8, P10V10, P10V12, P11V12, and P12V12 specimens exhibited a relatively high ΔT_{ad} (> 6 ℃), whereas P11V10, P12V10, and P13V12 had ΔT_{ad} less than 5 ℃. Specially, the P12V10 specimen showed the lowest ΔT_{ad} of 2.88 ℃, which was consistent with the above inference. Also, it was noted that the variation trend of the measured ΔT_{ad} with the process parameter was similar to that of the E_{rel} listed in Table 1. To better assess the energy conversion efficiency of the above specimens, COP_{mat} was calculated according to the following equation [29]:

$$COP_{mat} = \frac{Q}{\Delta E} = \left|\frac{mC_p\Delta T_{ad}}{V\int \sigma \mathrm{d}\varepsilon}\right| = \left|\frac{\rho C_p\Delta T_{ad}}{\int \sigma \mathrm{d}\varepsilon}\right|, \qquad (1)$$

where Q is the extracted latent heat, m denotes the specimen mass, V represents the specimen volume, C_p is the specific heat capacity (taken as 500 J·kg⁻¹·K⁻¹ in this study), and ρ designates the density (6.5 g·cm⁻³). From Eq. (1), a large ΔT_{ad} and a small ΔE will help achieve a high COP_{mat} value. The histograms with the COP_{mat} and ΔE values calculated for different process parameter combinations are plotted in Fig. 8(d). The P10V10 specimen exhibited the largest COP_{mat} of 4.89, which was accompanied by a small ΔE (4.45 MJ/m^3). Although P10V8 released the most energy during unloading (its E_{rel} reached 25.63 MJ/m^3), it also possessed the highest ΔE that led to a decrease in COP_{mat}.

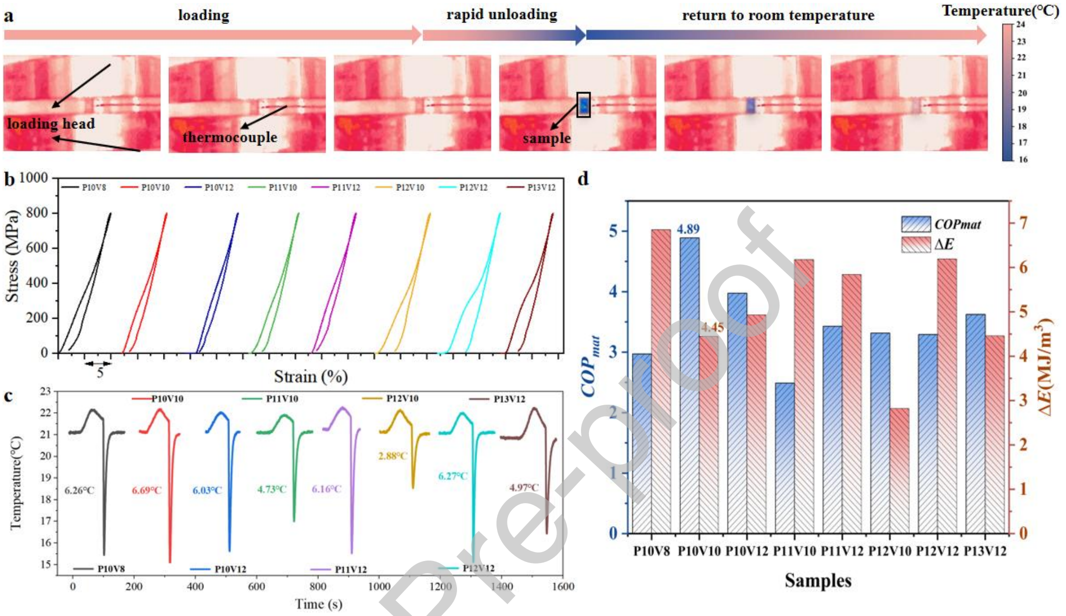

Fig. 8. Characterizations of elastocaloric properties: **(a)** Infrared temperature contour images of the P10V8 specimen at different loading/unloading stages; **(b)** The compressive loading–unloading curves; **(c)** Corresponding temperature change curves; **(d)** Calculated COP_{mat} and ΔE values.

3.4 One-way and two-way shape memory effect

According to the single cycle stress–strain curves in Fig. 5, the remaining 22 specimens failed to exhibit an apparent superelastic recovery phenomenon. Besides, the σ_c values of the remaining 22 specimens were found to be $\leqslant$ 208 MPa (Fig. 5(h)) and were mostly in the range of 100–150 MPa, thus revealing a sharp drop compared with those of the specimens chosen in Section 3.3. This implied that the detwinning/reorientation of martensite was more likely to dominate during the plateau period for these specimens [30]. Meanwhile, the ξ values after unloading without heating were also lower than 60% (Fig. 5(g)). These were < 50% when the applied *VED* exceeded 155.55 J/mm^3. Besides, from the perspective of the TTs (Fig. 3(i)), a large *VED* with high *P* and low *v* also tended to cause a higher M_f (> 0 ℃). To further determine the appropriate region with superior SME in the *P*-*v* plane, we tested the one-way shape memory strain ε_{ow} of these 22 specimens in the first cycle. ε_{ow} is defined as the strain change between the unloading state and heating state after unloading. Fig. 9a describes the mapping image of ε_{ow} in the *P*-*v* plane. The results show that the specimens fabricated at higher *P* and lower *v* were more prone to exhibit a relatively larger

ε_{ow}. For example, at v = 400 mm/s, all the specimens with P = 100, 110, 120, and 130 W achieved $\varepsilon_{ow} > 4\%$. For higher laser powers (P = 140 and 150 W), the specimens with v from 400 mm/s to 800 mm/s consistently showed $\varepsilon_{ow} > 4\%$. Combined with the results shown in Figs. 3(g) and 5(g), a region with considerable RT SME could be identified, which includes P10V4, P11V4, P12V4, P13V4, P14V4, P14V6, P14V8, P15V4, P15V6, and P15V8. We also studied the two-way shape memory properties of these 10 specimens.

Normally, achieving TWSME requires specific training procedures that involve repeated deformations and transformations. In this study, we obtained a stable TWSME mainly by a loading–unloading–heating–cooling training procedure, as shown in Fig. 9(b). Seven states were marked in a complete cycle, namely, state ① (zero stress at RT), state ② (loading to the maximum stress at RT), state ③ (unloading back to zero stress at RT), state ④ (heating to 120 ℃ after unloading), state ⑤ (holding the high temperature for 5 min without stress), state ⑥ (cooling to 0 ℃ without stress), and state ⑦ (back to RT without stress). Here, the strain change between stages ⑤ and ⑥ corresponds to ε_{tw}. Additionally, according to the evolution from state ④ to state ⑥, a large ε_{ow} is an essential precondition for achieving a considerable ε_{tw}. Fig. 9(c) shows the stress–strain curves of the selected specimens during 10 thermomechanical training cycles. After training, it was found that most of the specimens exhibited an increasing trend of ε_{ow} (Table S2), which was consistent with the observations of LPBF-fabricated NiTiHf systems reported by H.W. Ma et al. [31]. Furthermore, a quantitative analysis of the ε_{tw} in different training cycles was conducted (Fig. 9(d)), which revealed a progressive enhancement of ε_{tw} with an increase in the number of cycles. This might be attributed to the internal stress field induced by dislocations, which are always accompanied by phase transformation during training [32-34] and can serve as internal stress sources that regulate martensite variant selection through stress-field modulation [35], thereby triggering macroscopic two-way SME. With cumulative cycles, continued dislocation density elevation intensifies the internal stress fields, thereby activating more preferentially oriented martensite variants and thus contributing to a progressive increase in ε_{tw}. Notably, the P10V4 specimen demonstrated the largest ε_{tw} after 10 training cycles, reaching 2.15% (determined by caliper measurement) (Table S2). To obtain more precise results, TMA was employed further to characterize ε_{tw} (Fig. 9(e)). The results show that P10V4 still demonstrated the largest ε_{tw} (reaching 2.23%), whereas P15V8 exhibited a minimum value of 0.56%. This highlights the selective impact of the process parameters on training efficacy. Fig. 9(f) further depicts the variation in ε_{tw} with the applied *VED*. It was seen that ε_{tw} generally exhibited a trend of initial increase followed by a decrease with the *VED*, thus showing a relatively weak correlation. Notably, within the process window at v = 400 mm/s (the region highlighted by a red circle in Fig. 9(f)), ε_{tw} demonstrated an approximately linear correlation with laser power. The fitted relationship can be expressed as $\varepsilon_{tw} = -0.18P + 4.09$, with R^2 reaching 0.912. This indicates that ε_{tw} is inversely proportional to P and decreases by approximately 0.18%

per unit increase in P. According to the results in Fig. 3, an increase in P led to an increase in the TTs, which further indicated an enhancement in the Ni burning loss. In this case, fewer Ni-rich precipitates existed within the matrix, thereby weakening the interaction with dislocations and the corresponding internal stress field during the subsequent training process. Consequently, ε_{tw} decreased. For P14V8 and P15V8, a higher v may have induced more B2 phase retention in the matrix, thus deteriorating the two-way shape-memory properties.

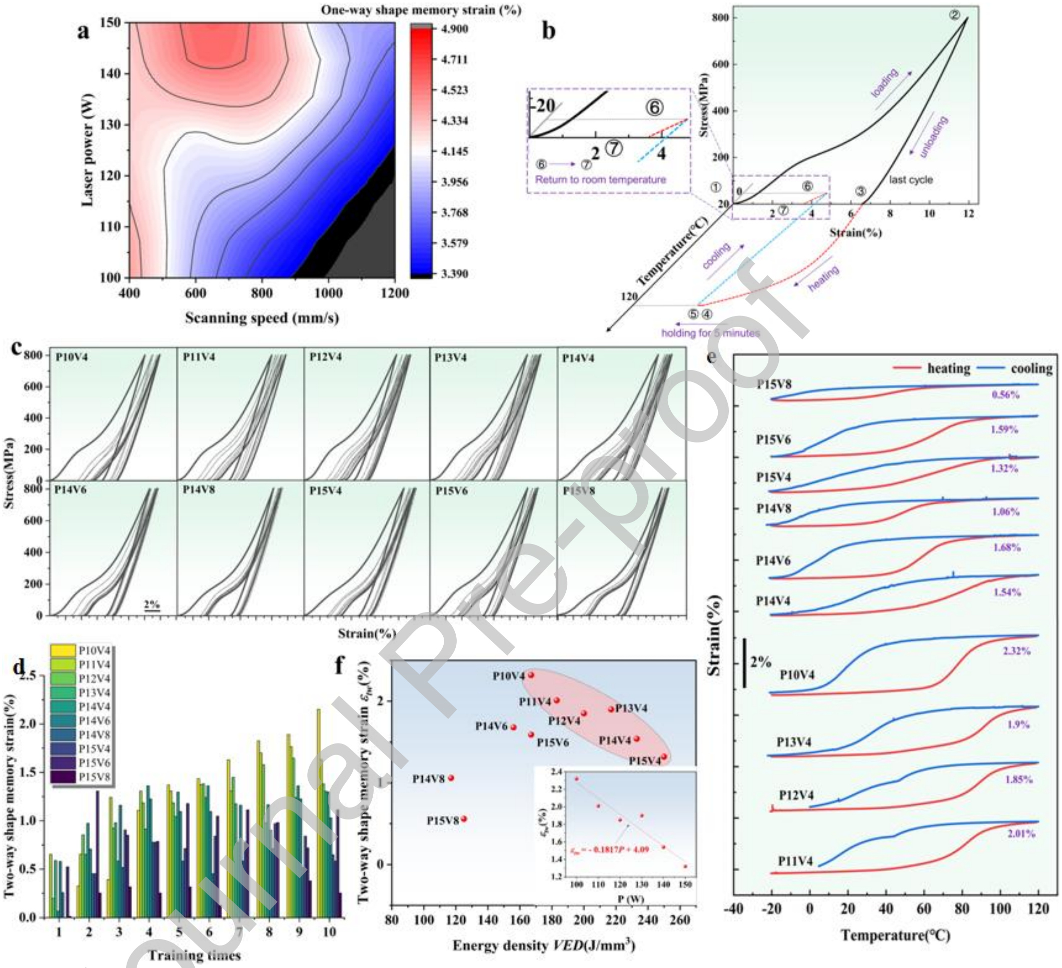

Fig. 9. Characterizations of shape memory properties: **(a)** ε_{ow} distribution map in P-v plane; **(b)** Schematic of the loading–unloading–heating–cooling training for obtaining TWSME; **(c)** Compressive stress–strain curves obtained during training; **(d)** Evolution of ε_{tw} with the training number; **(e)** ε_{tw} measured by TMA; **(f)** Evolution of ε_{tw} with *VED* and P.

4. Discussion

To design a heat-driven elastocaloric cooling system, a good TWSME with a large ε_{tw} for the heat actuator and an excellent eCE with a significant ΔT_{ad} for the elastocaloric refrigerator are necessary. Based on the above experimental results, it was found that the LPBF processing parameters play a prominent role in regulating the functional properties of NiTi alloys. Fig. 10 shows a functional differentiation diagram of the LPBF-fabricated Ni-rich NiTi alloys in the P-v plane. Three characteristic regions are evident: (1) region I, tends to display good RT SEM with a large ε_{ow} (> 4%); (2) region II, belongs to a transition region; (3) region III, tends to behave good RT

SE with a large ε_{rec} (> 8% in the first cycle). Moreover, according to the measured ΔT_{ad} and ε_{tw} values, two critical *VED* lines (namely, 66.7 J/mm^3 and 166.7 J/mm^3) can be determined roughly as the marked red and blue dotted lines, respectively. When the applied *VED* $\leqslant$ 66.7 J/mm^3, the specimen tended to achieve a significant ΔT_{ad} (> 6 ℃) during the RT eCE test. But an excessively low *VED* (e.g., $\leqslant$ 55.6 J/mm^3) can result in a deterioration of the densification degree (Fig. S1). Meanwhile, when the applied *VED* $\geqslant$ 166.7 J/mm^3, the specimen was more likely to possess a considerable ε_{tw} (> 1.3%). Also, an excessively high *VED* (e.g., $\geqslant$ 233.3 J/mm^3) would intensify the keyhole effect (Fig. S1). In particular, apart from *VED*, *v* plays a more dominant role in tailoring functional properties. As shown in Fig. 10, a considerable ε_{tw} is obtained mainly at v = 400 mm/s, while a significant ΔT_{ad} emerges mainly at v = 1200 mm/s. But when a much higher or much lower *P* is applied, *v* can be extended slightly to 600 mm/s in region I (e.g., the ε_{tw} of P14V6 reaches 1.68%) or reduced to 800 mm/s in region III (e.g., the ΔT_{ad} of P10V8 reaches 6.26 ℃). Essentially, this functional differentiation originates from variations in the thermal history and solidified microstructure caused by the laser processing parameters. If the distribution map of M_s and M_s-M_f and their sensitivity to the molten pool thermodynamics (Figs. 3(g) and 3(h)) are taken into account, it can be found that region I (especially the region with *VED* $\geqslant$ 166.7 J/mm^3) is mainly characterized by a severe Ni loss and heterogeneous microstructure, while region III is featured by less Ni loss but an even more heterogeneous microstructure. In the following sections, we will mainly discuss the influence mechanism of the laser energy input on the thermal behavior and solidified microstructure, the physical mechanism underlying functional differentiation manipulated by the laser beam, and a functional comparison based on three typical specimens (P10V4, P12V6, and P10V10, which correspond to the above-mentioned three different characteristic regions) (Fig. 10). Finally, the design and performance of a case study of a heat-driven elastocaloric cooling system using two groups of LPBF-fabricated NiTi-based double-helix springs is presented.

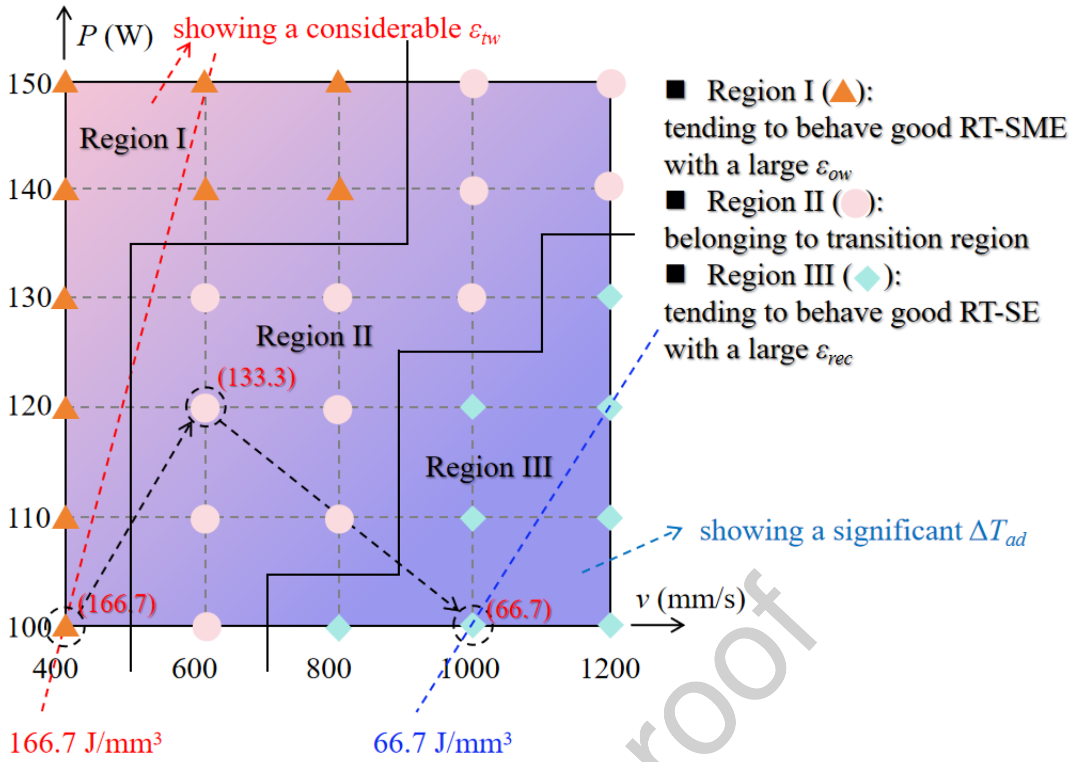

Fig. 10. Functional differentiation diagram of LPBF-fabricated NiTi alloys in a *P*-*v* plane.

4.1 Solidified microstructure feature and its tailoring principle involving laser energy input

To provide further insights into the origin of function differentiation induced by the LPBF processing parameters, the solidified microstructures of three typical specimens (P10V4, P12V6, and P10V10) were characterized further in detail. Fig. 11 shows the band contrast (BC) images, phase distribution maps, and inverse pole figures (IPFs) based on the EBSD method. Considering that the BC image was generated by measuring the quality of the diffraction pattern of each pixel point, it was observed that the P10V4 specimen showed a relatively low diffraction quality. This indicates that a severe lattice distortion existed in the P10V4 specimen. Alternative distributions of coarse grains (CGs) and fine grains (FGs) along the building direction (BD) were clearly observed in both P12V6 and P10V10 specimens. Furthermore, from the phase distribution maps, a much higher fraction of the B19' phase (reaching 8.22%) was found in the P10V4 specimen (which was mainly distributed within the zones with poor diffraction quality) compared with the 0.523% for the P12V6 specimen and 1.74% for the P10V10 specimen. The difference in the content of the retained B19' phase may be mainly determined from the various Ni burning losses induced by the different laser energy inputs. According to Fig. 3, the TTs (A_f and M_f) of P10V4 specimen increased substantially (by 47.3 ℃ and 46.7 ℃, respectively) compared with the P10V10 specimen. Therefore, a serious Ni loss occurred in the P10V4 specimen, which effectively decreased the martensitic transformation barrier and consequently caused the retention of more B19' phase. Subsequently, the grain orientation distribution was studied. All the three specimens exhibited a considerable maximum texture index n_{max} (> 7). This indicates that there was a certain preferred orientation for each specimen. At a relatively higher *VED* of 166.7 J/mm^3, $n_{\max}$ reached 19.96, thus showing a strong orientation texture. Meanwhile, $\{001\}_{B2}$ was found to be preferentially oriented at approximately 45° with the Y_0-axis (parallel to BD). As the *VED* decreased to 133.3 J/mm^3 (P12V6), $n_{\max}$ reduced significantly (by 38.63%), and the preferential orientation deviation angle of $\{001\}_{B2}$ with the BD changed slightly to ~30°. When the applied *VED* was decreased further to 66.7 J/mm^3 (P10V10), $n_{\max}$ also decreased to 7.34. However, the preferential orientation of $\{001\}_{B2}$ was deflected to be closely parallel to the BD. This transformation of the grain orientation is believed to play an important role in tailoring the functional properties of LPBF-fabricated NiTi alloys.

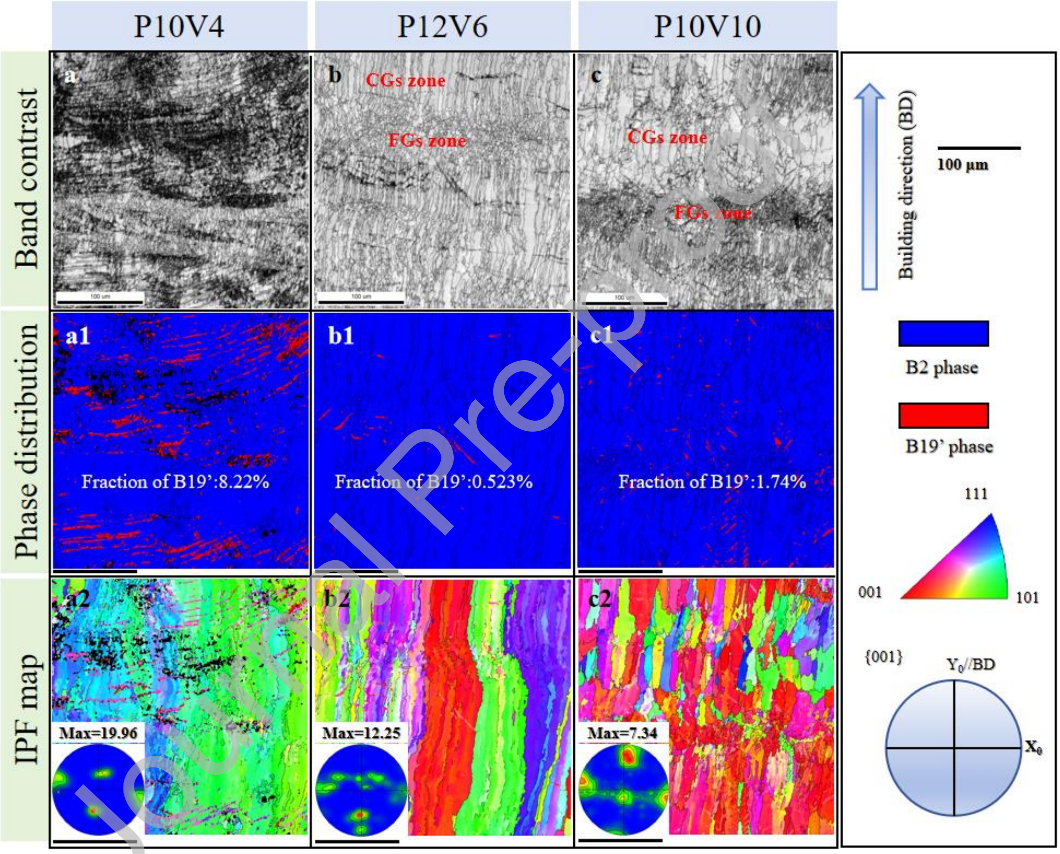

Fig. 11. Phase distributions and grain orientation features obtained by EBSD: **(a-c)** Band contrast (BD) images; **(a1-c1)** Phase distribution maps; **(a2-c2)** IPFs maps with inserted pole figures (PFs).

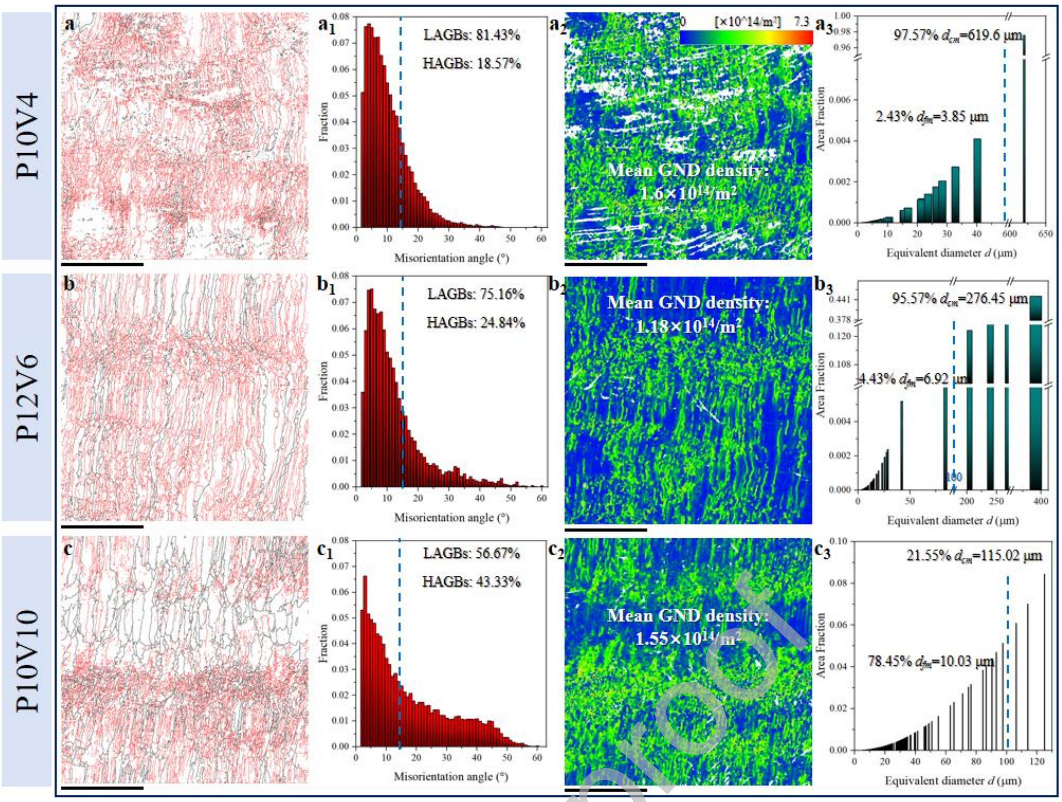

Fig. 12. Analysis of grain boundary, dislocation density, and grain size: **(a-c)** Misorientation distribution maps; **(a1-c1)** Statistical histograms of misorientation angle; **(a2-c2)** GND density distribution maps; **(a3-c3)** Statistical histograms of grain size distribution.

Fig. 12 shows the misorientation distribution maps, geometrically necessary dislocation (GND) density distribution maps, and statistical histograms of the grain size and misorientation angle. The results suggest that low-angle grain boundaries (LAGBs, 2–15°, red lines) dominated absolutely at *VED* = 166.7 J/mm^3, occupying 81.43% (Figs. 12(a) and (a1)). Normally, LAGBs are regarded as an array of dislocations [36] that originate from many factors such as supersaturated Ni atoms and the considerable residual stress closely associated with the nature of the LPBF process. Hence, the P10V4 specimen exhibited a high dislocation density. According to the GND density distribution pattern (Fig. 12(a2)), the mean GND density was measured as 3.2 × 10^{14}/m^2. In addition, it was found that the areas with high GND density and the positions where LAGBs emerged overlapped significantly. Due to the high fraction of LAGBs, the grain sizes were mainly concentrated within the range of > 100 μm (regarded here as a critical size of CGs and FGs). As shown in Fig. 12(a3), the grain size of 619.6 μm took up 97.57% of the area. When *VED* became 133.3 J/mm^3, the fraction of LAGBs decreased slightly to 75.16%, and many continuous and slender high-angle grain boundaries (HAGBs) were clearly visible (Fig. 12(b) and (b1)). Accordingly, the mean GND density fell to 1.18 × 10^{14}/m^2 (Fig. 12(b2)), thus possibly indicating a significant decrease in the residual stress in this case. Moreover, the average grain size d_{cm} of the CG zone was reduced remarkably (by 55.38%), although the area fraction remained above 95% (Fig. 12(b3)). When a lower *VED* of 66.7 J/mm^3 was applied, a sharp decrease in the fraction of LAGBs occurred. As a result, it was clearly observed that the density of LAGBs within the CG zone decreased greatly (Fig. 12(c)). More LAGBs were present in the FG zone. However, the mean GND density was reversely elevated to $1.55 \times 10^{14}/m^2$ (Fig. 12(c2)), rather than declining correspondingly with *VED*. More importantly, FGs dominated the solidified microstructure. The area fraction of FGs with an equivalent diameter of < 100 μm reached 78.45%, and the average size d_{fm} in the FGs zone was 10.03 μm (Fig. 12(c3)).

Normally, the development of a solidified microstructure is closely associated with the thermal history of the LPBF. On this basis, we monitored the temperature evolution of the LPBF-fabricated NiTi specimens under different processing parameters using an infrared camera. The monitored data for successive 20 layers at a low temperature range of 700–1500 ℃ were recorded and plotted, as shown in Figs. 13(a-c). Considering that the monitored maximum temperature approached the liquid line of the NiTi alloy, the integrated area under the thermal history curve was regarded as the total heat input (*THI*) required to sustain grain growth over time [22]. According to the calculations, the average *THI* value is proportional to the applied *VED* (Fig. 13(d)). It was also found that the average grain size d_m ($= f_1 d_{fm} + f_2 d_{cm}$, where f_1 and f_2 are the area fractions of the FGs and CGs, respectively) demonstrated a highly linear relationship with the average *THI* ($R^2 > 0.95$), which could be expressed as $d_m = 1.7THI - 440.8$ (Fig. 13(e)). This suggests that the grain size can be tailored precisely by controlling the processing parameters and resultant *THI*s. Furthermore, the cooling rate was calculated by taking the derivative of the *T*-*t* curve. Obviously, P10V10 had the highest cooling rate of 6.1×10^3 ℃/s, while P10V4 presented the lowest cooling rate of 5.1×10^3 ℃/s (Fig. 13(f)). Normally, a high cooling rate implies a stronger undercooling and a higher nucleation rate, which trigger the formation of finer grains. Therefore, the cooling rate evolution accounts for the average grain-size change with *VED*. Fig. 13(g) presents a schematic of the formation mechanism of the heterogeneous microstructure. Within a laser-induced molten pool, the G / R value (G is the temperature gradient and R is the solidification rate) always tends to show a maximum value at the bottom of the molten pool and a minimum value at the top of the molten pool [37, 38]. According to the solidification map [39], columnar dendrites grow preferentially at the bottom of the molten pool, and equiaxed grains are prone to form in the top region. During the subsequent molten-pool overlap process (including the overlap between adjacent tracks and layers), the fine equiaxed grains were more susceptible to dissolution. This can be explained by the Ostwald ripening effect [22]. It drives the combination of these fine equiaxed grains around the new molten pool boundary into larger grains via solute atom diffusion. In the case of a high *THI* (e.g., P10V4), fewer fine equiaxed grains were retained. Meanwhile, our previous work proved that a considerable thermal stress tends to emerge in the molten pool bottom [40], which is therefore able to facilitate the transformation of B2→B19’ during the final stage of solidification (e.g., the B19’ phase observed in Fig. 11). For the P12V6 specimen, a higher *P* and higher *v* resulted in a wider and shallower molten pool compared with the

P10V4 specimen. Under this condition, the overlapping region between adjacent tracks increased in size, whereas that between adjacent layers decreased. However, the *THI* values remained high. Therefore, CGs dominated in this case. For the P10V10 specimen, the energy density decreased significantly, thereby yielding a small and shallow molten pool. Consequently, the overlapping regions reduced, and the Ostwald ripening effect faded. Under these conditions, the FGs regions became more significant than the CGs region. Regarding the B19' phase, compared with the P10V4 specimen, the fraction of B19' in P10V10 decreased sharply. Using a simulation method, Chen et al. found that an increase in *v* could induce a reduction in *G* by the simulation method [41]. This means that a high *v* could lead to a decrease in thermal stress, thus suppressing the subsequent martensite transformation.

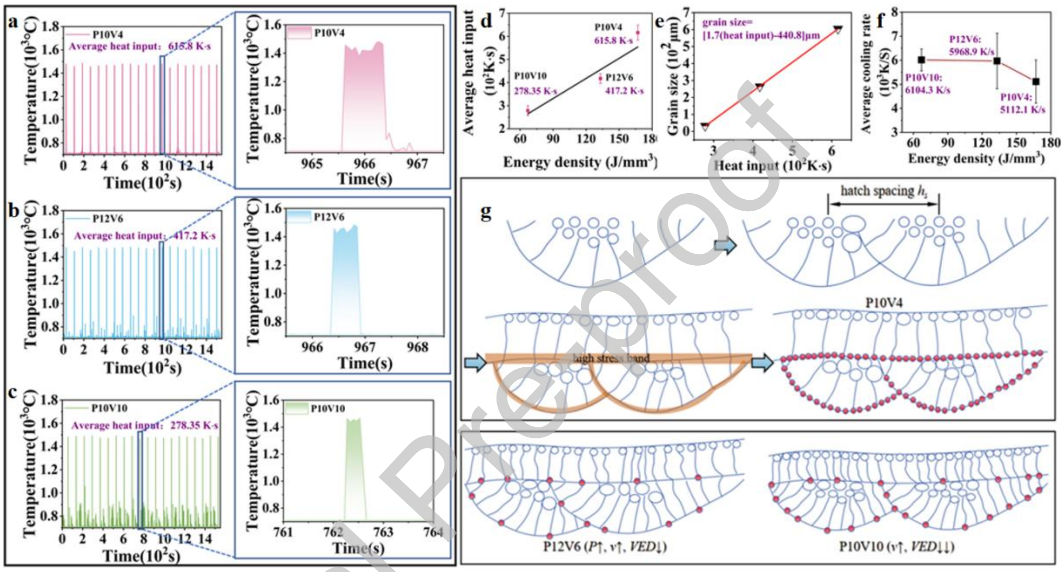

Fig. 13. Microstructural evolution mechanism: **(a-c)** *T-t* evolution curves of the molten pool monitored at a low temperature range of 700–1500 ℃ via an infrared camera; **(d)** Relationship between average *THI* and *VED*; **(e)** Relationship between average grain size and *THI*; **(f)** Variation in average cooling rate with the *VED*; **(g)** Schematic of formation mechanism of a heterogeneous microstructure.

4.2 Physical mechanisms of functional differentiation induced by laser energy input

From the perspective of the functional behavior of NiTi alloys, the key indicator is the critical temperature T_A for the reverse transformation. When T_A is close to or below the RT, reverse transformation can occur spontaneously without an extra thermal stimulus, with the specimen behaving as RT-SE. When T_A is higher than RT, an extra thermal stimulus is required to drive the reverse transformation. Under these conditions, the specimen is more inclined to behave as an RT-SME. T_A can be determined according to the thermodynamic relationship of the reverse transformation [42]:

$$\Delta G^{M-A} = \Delta H^{M-A} - T_A \Delta S^{M-A}_{stress} - \Delta G^{M-A}_{mech} + \Delta E^{M-A}_{el} + \Delta E^{M-A}_{ir} = 0, \tag{2}$$

where $\Delta S_{stress}{}^{M\text{-}A}$ is the stress-released transformation entropy, $\Delta G_{mech}{}^{M\text{-}A}$ is the mechanical energy released during the reverse transformation, $\Delta E_{el}{}^{M\text{-}A}$ is the elastic strain energy, and $\Delta E_{ir}{}^{M\text{-}A}$ is the inelastic strain or friction energy.

Hence, T_A can be expressed as follows:

$$T_A = \frac{\Delta H^{M-A} - \Delta G_{mech}^{M-A} + \Delta E_{el}^{M-A} + \Delta E_{ir}^{M-A}}{\Delta S_{stress}^{M-A}}. \tag{3}$$

From the above equation, it is seen that T_A is influenced directly by $\Delta H^{M\text{-}A}$, $\Delta G_{mech}^{M\text{-}A}$, $\Delta E_{el}^{M\text{-}A}$, $\Delta E_{ir}^{M\text{-}A}$, and $\Delta S_{stress}^{M\text{-}A}$. All the five items are dependent on the solidified microstructure tailored by the laser processing parameters, parts of which can be described further as follows [42]:

$$\Delta G_{mech} = \frac{1}{\rho}\int \sigma_{app}\mathrm{d}\varepsilon, \tag{4}$$

$$\Delta E_{el}^{M-A} = -\frac{1}{2\rho}\int \sigma_{ij}^{t}\varepsilon_{ij}^{t}\mathrm{d}f - \frac{1}{\rho}\int \sigma_{ij}^{d}\varepsilon_{ij}^{t}\mathrm{d}f, \tag{5}$$

$$\Delta E_{ir}^{M-A} = \frac{\sigma_{hy}\varepsilon_{tr}}{2\rho}, \tag{6}$$

$$\Delta S_{stress}^{M-A} = -\frac{\varepsilon_{tr}^{M-A}}{\rho}\frac{\mathrm{d}\sigma_{tr}}{\mathrm{d}T}, \tag{7}$$

where σ_{app} is the applied stress; σ_{ij}^{t} (or σ_{tr}) and σ_{ij}^{d} are the internal stress caused by the transformation and the defects or precipitates, respectively; ε_{ij}^{t} or ε_{tr} denotes the transformation strain; σ_{hy} is the stress hysteresis; ρ is the material density; and $\mathrm{d}f = \mathrm{d}V/V$ (here V is the volume of the specimen). To calculate $\Delta S_{stress}^{M\text{-}A}$, the loading–unloading behavior at different operation temperature was evaluated, as shown in Figs. 14(a-c). Then, the σ_{tr}-T relationship curve was plotted (Fig. 14(d)). It was found that $d\sigma_{tr}/dT$ can be fitted as a constant, thus showing a typical characteristic of first-order martensitic phase transformation. In particular, for P10V4, a fast transition from a typical SME to an excellent SE with small stress hysteresis was observed when the temperature increased from 60 ℃ to 70 ℃. Here, 70 ℃ can be regarded as the quasi critical temperature of P10V4. It is apparently higher than the A_s (43.5℃) measured without stress. Subsequently, the $\Delta S_{stress}^{M\text{-}A}$ at different temperatures, as well as the $\Delta G_{mech}^{M\text{-}A}$ and $\Delta E_{ir}^{M\text{-}A}$ at the quasi critical temperature, were calculated and plotted (Figs. 14(e) and 14(f)). The results show that P10V10 possessed the largest $\Delta S_{stress}^{M\text{-}A}$, whereas the other two specimens exhibited similar but lower $\Delta S_{stress}^{M\text{-}A}$. Meanwhile, the ($\Delta H^{M\text{-}A}$ - $\Delta G_{mech}^{M\text{-}A}$ + $\Delta E_{ir}^{M\text{-}A}$) values for P10V4, P12V6, and P10V10 are 21.158 J/g, 19.744 J/g, and 17.518 J/g, respectively. Hence, the comparison of T_A will depend mainly on $\Delta E_{el}^{M\text{-}A}$. According to Eq. (5), the $\Delta E_{el}^{M\text{-}A}$ value is primarily controlled by σ_{tr}, ε_{tr}, and σ_{ij}^{d}, which are closely associated with the solidified microstructure features. In this condition, the effects of a solidified microstructure on the main variables in the expression of $\Delta E_{el}^{M\text{-}A}$ are discussed in terms of the following four aspects to determine their distinct T_A and resultant function difference at RT.

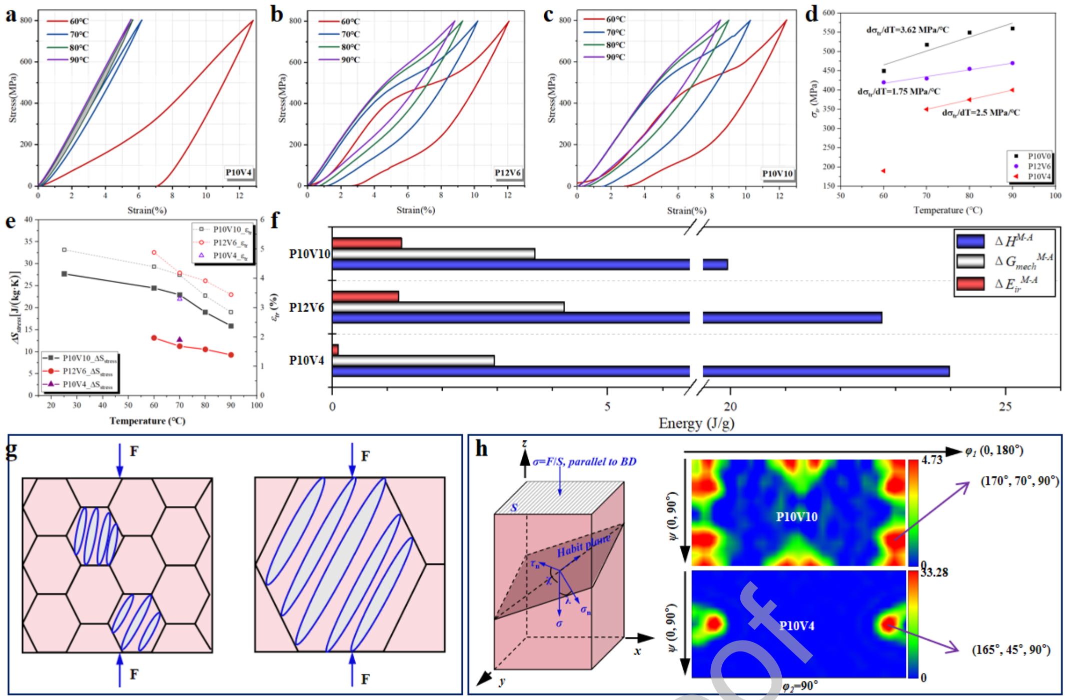

Fig. 14. Analysis of influencing factors determining the critical temperature T_A for the reverse transformation: **(a-c)** Compressive loading–unloading curves at different testing temperatures for P10V4, P12V6, and P10V10; **(d)** Fitted dσ/dT relationship; **e** calculated $\Delta S_{stress}{}^{M\text{-}A}$ and ε_{tr}; **(f)** Histograms of $\Delta H^{M\text{-}A}$, $\Delta G_{mech}{}^{M\text{-}A}$, and $\Delta E_{ir}{}^{M\text{-}A}$ for the three specimens; **(g)** Effect of grain size on $\Delta E_{el}{}^{M\text{-}A}$; **(h)** Effect of grain orientation on $\Delta E_{el}{}^{M\text{-}A}$.

(i) *Ni content.*

Owing to the distinct differences in the boiling points and saturation vapor pressures of Ni and Ti, burning loss of Ni becomes almost inevitable during the LPBF process of NiTi-based alloys. Various laser energy inputs yielded different degrees of Ni loss. Notably, the change in Ni content can directly influence the phase transformation behavior. It is well known that a low Ni content can result in increases in TTs, considering that Ni is a stabilizing element of the B2 phase [17]. Additionally, it has been reported that an increase in Ni content can result in a marginal reduction in the β of the B19' lattice, thus decreasing the difference in lattice geometry between the B2 and B19' phases [43]. In this case, the structural entropy change between B2 and B19' decreased (Fig. 4(f)) [44], thereby further inducing a decrease in enthalpy variation. This partly accounts for the lower ΔH of P10V10 than that of P10V4, considering the higher Ni content in P10V10. Furthermore, the Ni content also has a significant effect on ε_{tr}. Zhou et al. pointed out that ε_{tr} is proportional to the deviation Δc(Ni) of the Ni concentration from the equilibrium value [45]. Obviously, the Δc(Ni) for P10V10 is larger due to the lower Ni burning loss, thereby contributing to a higher ε_{tr} and the resultant larger $|\Delta E_{el}{}^{M\text{-}A}|$ and $\Delta E_{ir}{}^{M\text{-}A}$.

(ii) *Grain size*.

Many studies have focused on the influence of grain size on martensitic phase transformation [46-48]. It has been found that a decrease in grain size can lead to an increase in σ_{tr} [48]. The finer grains indicate a larger fraction of grain boundaries, which results in a greater transformation barrier, as shown in Fig. 14(g). According to the results in Fig. 12, the average grain sizes of P10V4 and P10V10 were 604.64 μm and 32.66 μm, respectively. Correspondingly, the fraction of HAGBs in P10V10 increased by 133.33% compared with that in P10V4. In this condition, the P10V10 specimen inevitably displayed a higher transformation barrier and resultant higher σ_{tr} and $|\Delta E_{el}^{M\text{-}A}|$. Notably, during the reverse transformation, ΔE_{el} can act as the driving force due to its negative value. Hence, a higher $|\Delta E_{el}^{M\text{-}A}|$ value is conducive to the spontaneous occurrence of reverse transformation at RT.

(iii) ***Grain orientation***.

Liu et al. studied the shape-recovery behavior of LPBF-fabricated NiTi alloys and found that the martensitic transformation was related to the grain-orientation spread distribution [49]. Similar to the plastic deformation, the B2→B19' transformation also follows Schmid's law. The B19' phase is formed by shear in the directions of <0.4580, 0.7706, and 0.4432> on the habit planes of {-0.8684, 0.2688, and 0.4138} [50]. Fig. 14(h) shows a schematic of the decomposition of the applied compressive stress σ along the shear direction (τ_n) and the normal direction (σ_n) to the habit plane. The angles between these directions are denoted by χ and λ. Hence, the Schmid factor m can be determined by the equation $m = \cos\chi \cdot \cos\lambda$. A large m value facilitates the stress-induced martensite transformation (SIMT). To calculate m, the vectors in the specimen coordinate system of the shear system must be obtained. Fig. 14(h) further presents the orientation distribution function (ODF) images of the B2 phase at $\varphi_2 = 90°$. It is seen that P10V10 was mainly concentrated in the (15°, 20°, 90°), (15°, 70°, 90°), (170°, 20°, 90°), and (170°, 70°, 90°) orientations, whereas P10V4 was mainly concentrated in the (20°, 45°, 90°) and (165°, 45°, 90°) orientations. Using rotation matrix transformation, the average m values for P10V10 and P10V4 were calculated to be 0.385 and 0.407, respectively. This suggests that it was more difficult for P10V10 to undergo martensitic transformation, thus resulting in increases in σ_{tr} and $|\Delta E_{el}^{M\text{-}A}|$.

(iv) ***Dislocation and precipitation***.

According to Eq. (11), the stress field induced by defects such as dislocations and precipitates also plays a non-negligible role in driving the reverse transformation. Fig. 15 shows the TEM results for the P10V4 and P10V10 specimens. For P10V4, a microstructure with typical coarsened columnar grains and local self-accommodating martensitic twins was observed (Figs. 15(a-a2)). In addition, some irregular nanoprecipitates were observed along the subgrain boundaries, as shown in Fig. 15(a3). Calculations revealed that the precipitation density reached $1.20 \times 10^{20}/m^3$. Then, the EDS mapping results (Figs. 15(a4-a7)) indicated that these nanoprecipitates were $Ti_4Ni_2O_x$, which was consistent with our previous report [40]. Moreover, we rebuilt the strain distribution in Fig. 15(a8) containing a nanoprecipitate particle based on a geometric phase analysis (GPA). From the distribution of strain tensor ε_{xy} (Fig.

15(a9)), it was found that the precipitation of $Ti_4Ni_2O_x$ nanoparticles caused obvious strain fluctuations within the surrounding matrix. In contrast, the P10V10 specimen exhibited a nearly B2-dominated microstructure with finer grains (Figs. 15(b-b2)). In addition, a larger precipitation density of $1.86 \times 10^{21}/m^3$ and finer precipitation size (average radius of ~12 nm) were observed (Fig. 15(b3)). The strain fluctuations induced by $Ti_4Ni_2O_x$ nanoparticles were greater than those induced by P10V4 (Fig. 15(b9)). Therefore, the enhanced strain fluctuations in P10V10 can elevate the internal stress σ^d and corresponding $|\Delta E_{el}^{M\text{-}A}|$.

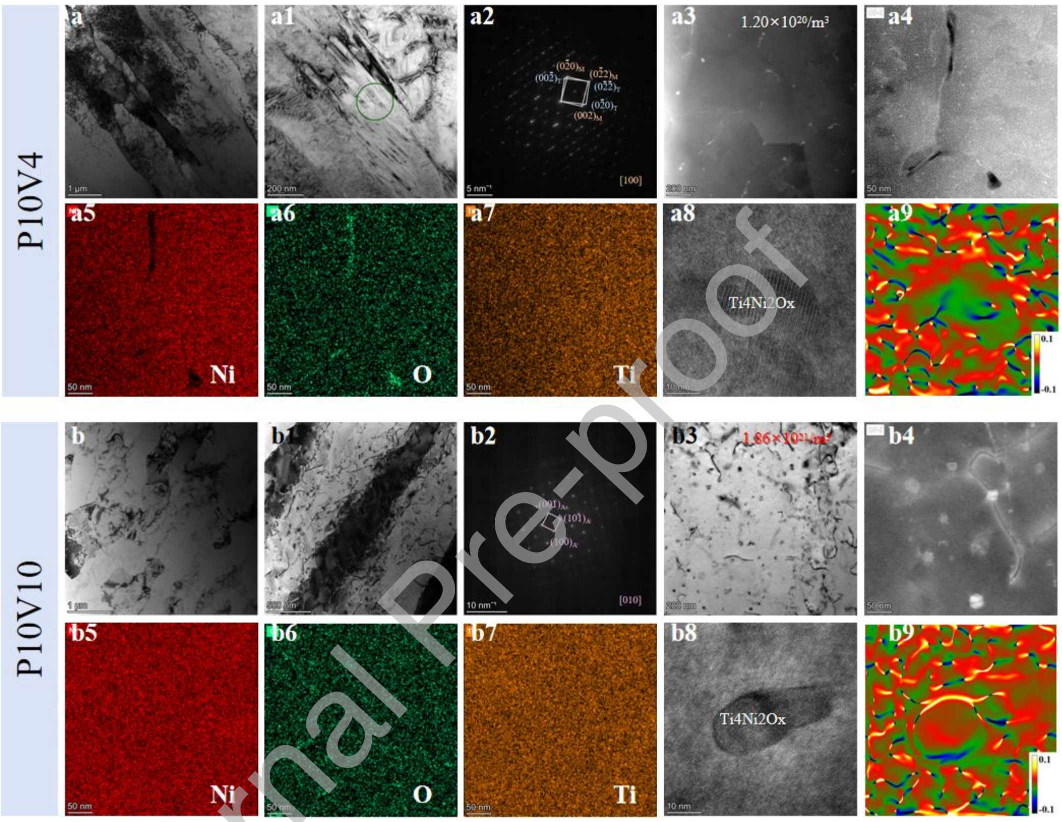

Fig. 15. TEM characterizations of P10V10 and P10V4 specimens: **(a, b)** Low-magnification image showing the matrix microstructure; **(a1**, **a2**, **b1**, **b2)** Self-accommodation martensitic twins and corresponding selected area diffraction pattern (SADP); **(a3-a7**, **b3-b7)** Detected nanoprecipitates and corresponding EDS mapping images; **(a8**, **a9**, **b8**, **b9)** HRTEM images of the nanoprecipitate and corresponding distribution maps of strain tensor ε_{xy}.

Based on the above analysis, P10V10 has an apparently larger $|\Delta E_{el}^{M\text{-}A}|$ that therefore provides the greater driving force for the reverse transformation. Under these conditions, a low T_A was obtained for P10V10, thereby leading to an increase in SE at RT. In contrast, P10V4 had the largest T_A (which demanded a considerable thermal stimulus to activate the reverse transformation) and consequently behaved as an RT-SME.

4.3 Comparison of functional properties

According to the results in Section 3.3 and 3.4, the P10V10 and P10V4 specimens demonstrated optimized eCE and SME performances, respectively. To better evaluate the functional properties obtained in our work, we further compared them with the NiTi-based alloys reported in other investigations. As for the eCE performance, the most critical indicator is ΔT_{ad}. In this work, the optimized largest ΔT_{ad} was 6.69 K (measured in P10V10). But it is far lower than the corresponding theoretical value (approximately 16.79 K, calculated by $\Delta T_{ad}^{theory} = (\varepsilon_{tr} \cdot T \cdot (\mathrm{d}\sigma_{tr}/\mathrm{d}T)) / (\rho \cdot C_p))$. Because the testing temperature (RT) was lower than A_f, the volume involved in the phase transformation was restricted. Meanwhile, the temperature rise induced by the dissipation work ΔE also resulted in the difference [51]. Besides, the second indicator we chose was σ_{app} rather than ε_{app}, considering the increasing demand of the low drive force [10]. The comparison results of ΔT_{ad}-σ_{app} are displayed in Fig. 16(a). To enhance the comparison, all the NiTi-based alloys were obtained using additive manufacturing methods, and all the eCE tests were performed at RT. To the best of our knowledge, our results show a high elastocaloric strength ($|\Delta T_{ad} / \sigma_{app}|$) compared with those of NiTi-based alloys fabricated by laser melting deposition (LMD) [18, 52-56] or wire arc additive manufacturing (WAAM) [57]. But comparing with parts of LPBF-fabricated NiTi alloys [21, 22, 58], our results present some disadvantages, which might be attributed to the existing larger σ_{tr} that can be derived from the finer grain size and high density of nanoscale precipitates.

As for the SME performance, we focused primarily on ε_{ow} and ε_{tw}. According to the results in Fig. 9, the optimized ε_{ow} and ε_{tw} (emerging in P10V4) in this work reached 4.95% and 2.23%, respectively. Fig. 16b compares our work with the literature data, including conventionally processed NiTi alloys [59-61], NiTiCu alloys [62], NiTiNbFe alloys [63], NiTiHf alloys [64], NiTiHfCu alloys [65], and NiTiNbCu alloys [66], as well as LPBF-fabricated NiTi-based alloys [23, 31]. The data from this study are located in the upper-right region of the comparative plot and show the simultaneous enhancement of one-way and two-way shape-memory performance. According to the results shown in Fig. 12, the P10V4 specimen had a high fraction of LAGBs and a high dislocation density. During the loading process, these dislocations acted as nucleation sites to facilitate the formation of preferential martensite variants along the loading direction. Meanwhile, owing to the small amount of martensite in the initial solidified microstructure, detwinning or reorientation of the pre-existing martensite occurred easily. In addition, the high density of dislocations and numerous nanoscale $Ti_4Ni_2O_x$ precipitates also enhanced the matrix, thereby suppressing the production of an irrecoverable strain. All of these contributed to a relatively considerable ε_{ow}. Then, by successive training of loading, unloading, heating, and cooling, pre-existing dislocations were activated and aligned on specific crystal planes [23], thus yielding directional internal stress fields that could be intensified further by the interaction between the dislocation array and $Ti_4Ni_2O_x$ nanoprecipitates. Subsequently, these newly created large internal stress fields preferentially activated martensite variants with favorable orientations, thus establishing the prerequisite for the large ε_{tw} attained in this study.

Based on the above discussion, we preliminarily realized microstructure-derived functional differentiation via laser energy manipulation and synchronously achieved a relatively high eCE and superior TWSME. This tailoring strategy can be further transferred to the LPBF additive manufacturing of complex macroscopic structures (e.g., double helix springs and torsion–compression coupling structures) with differentiated microstructural features (Fig. 16(c)). In the following section, we attempt to build a simple cascade architecture using two groups of NiTi-based double-helix springs fabricated by LPBF using various laser energy densities to verify the feasibility of heat-driven elastocaloric cooling.

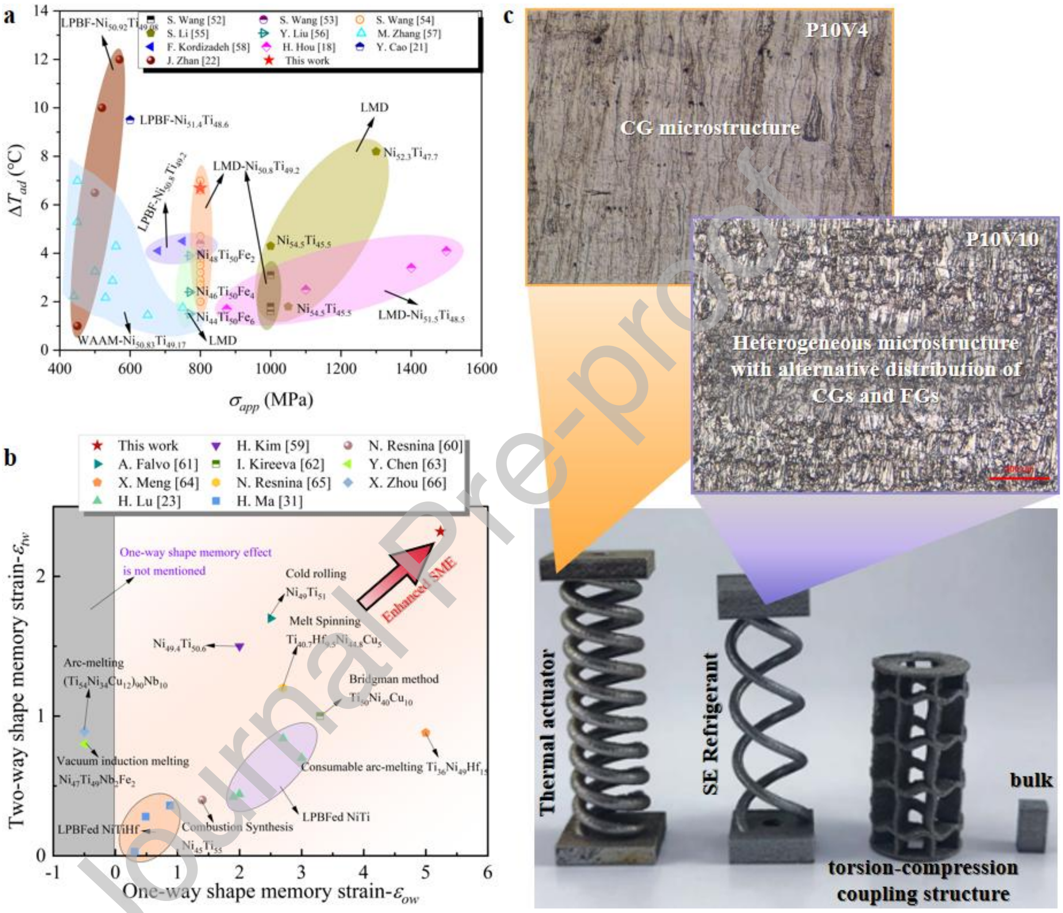

Fig. 16. Advantages of LPBF-fabricated NiTi alloys with various microstructure features: **(a)** Comparison of cooling performance in this work with that of additive manufactured NiTi-based alloys in other studies; **(b)** Comparison of shape memory properties in this work with the reported NiTi-based alloys in other studies; **(c)** Application of microstructure-derived functional differentiation via laser energy manipulation in the LPBF of NiTi-based complex structures.

4.4 Case study

Fig. 17(a) shows such a cascade architecture consisting of two groups of laser-additive-manufactured NiTi-based double-helix structures. The one on the left is fabricated using a high-energy input (P10V4) and serves as a thermal actuator, whereas the one on the right is processed at a low-energy input (P10V10) and acts as a superelastic refrigerant. In addition, to enhance the TWSME of the actuator spring, constrained aging was employed instead of pre-deformation because Ni_4Ti_3 precipitates tend to induce larger localized stress fields. The constrained aging procedure comprised the following steps: (1) compressing the actuator spring to a prescribed displacement; (2) securing it in a constraining fixture; (3) aging in a vacuum furnace at 500 °C for 1 h; and (4) subsequent furnace cooling. Then, the aged actuator spring was subjected to 12 thermal cycles to stabilize its TWSME performance. Fig. 17(b) shows the evolution of the two-way shape memory displacement with respect to the number of thermal cycles. The results show that the two-way shape memory displacement increased progressively with the number of cycles and ultimately attained 4.5 mm.

Subsequently, the aged actuator and refrigerant springs were assembled into a heat-driven elastocaloric cooling cascade architecture (Fig. 17(c)) to evaluate the multieffect coupled refrigeration performance. The operational principle is aligned with the schematic shown in Figure 17(a). To eliminate environmental thermal interference, the refrigerant spring on the left side was wrapped with thermal insulation, and its temperature variation was monitored using thermocouples. The right-side actuator spring was activated by hot air and liquid-nitrogen cooling. The experimental protocol is shown in Supplementary Video.

To better illustrate the effectiveness of the thermal actuator, the temperature change curves of the refrigerant spring under different driving conditions (i.e., the normal mechanical actuator and the proposed thermal actuator in this study) were recorded, as shown in Figs. 17(d) and 17(e). The results demonstrated that the refrigerant spring generated a ΔT_{ad} of 0.75 °C by the thermal actuator, which was marginally lower than that (1.07 °C) produced by the normal mechanical loading. This discrepancy may be attributed to the relatively slow actuation response rate of the actuator spring combined with the frictional dissipation between the intermediate linkage and sliding rails. Although the temperature change caused by the thermal actuator was modest, it validated the feasibility of the proposed thermally driven refrigeration model. By optimizing the elastocaloric structures and actuating properties in future studies, a practical compact multifunctional coupled elastocaloric refrigeration device based on LAM can be developed.

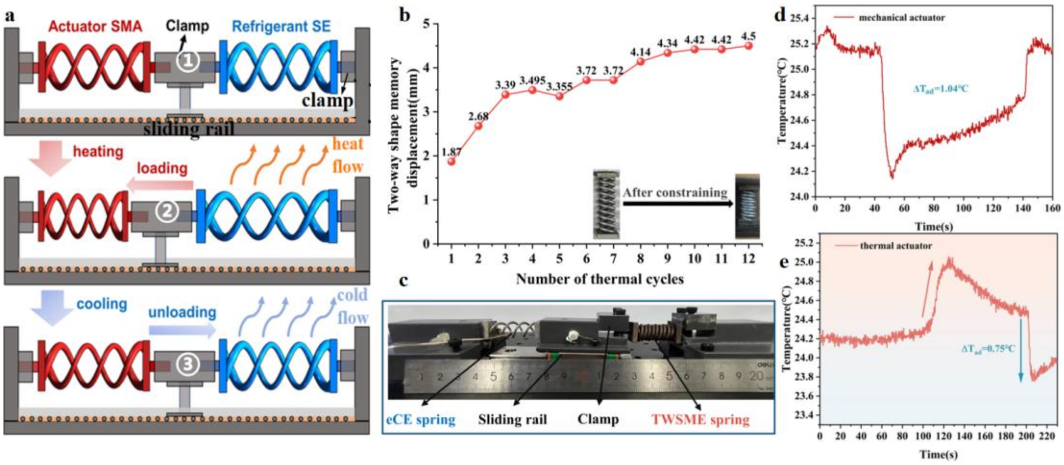

Fig. 17. Proposed heat-driven elastocaloric cooling device mode and corresponding experimental verification: (**a**) Schematic of the proposed simple heat-driven cascade architecture and its main working stages including ① the initial state with zero stress in the actuator SMA and refrigerant SA; ② heating of the actuator SMA and loading of the refrigerant SA, which cause the heat release in the refrigerant SA; ③ cooling of the actuator SMA and unloading of the refrigerant SA, which cause the heat absorption in the refrigerant SA; (**b**) Evolution of two-way shape memory displacement during thermal cycles; (**c**) Thermally actuated elastocaloric device; (**d**) Temperature variation curve obtained via mechanical testing; (**e**) Temperature variation curve obtained by thermal actuator.

5. Conclusions

This study systematically investigated the effects of laser processing parameters on the phase transformation behavior, mechanical response behavior, and functional properties of LPBF-fabricated Ni-rich NiTi alloys. Microstructure-derived functional differentiation via laser energy manipulation contributed to the formation of a relatively high eCE and a superior TWSME. Furthermore, a multi-effect-coupled thermally driven elastocaloric cooling device was proposed and verified. The main conclusions of this study are as follows:

(1) A low *VED* combined with a low P and high v tended to result in low TTs, whereas a high *VED* combined with a high P and low v was more likely to result in high TTs. The TTs were more sensitive to the applied v than to P.

(2) A functional differentiation diagram of the LPBF-fabricated Ni-rich NiTi alloys in the P-v plane was established. At 55.6 J/mm^3 $\leqslant$ *VED* $\leqslant$ 66.7 J/mm^3, the specimen tended to achieve a significant ΔT_{ad} (> 6 ℃). At 166.7 J/mm^3 $\leqslant$ *VED* $\leqslant$ 233.3 J/mm^3, the specimen was more likely to possess a considerable ε_{tw} (> 1.3%). Specially, P10V10 showed the largest ΔT_{ad} of 6.69 °C, and P10V4 demonstrated the most considerable ε_{tw} of 2.23% after 10 training cycles.

(3) The specimen with considerable RT eCE possessed a heterogeneous microstructure with an alternating distribution of CGs and FGs, whereas the specimen with superior TWSME was mainly characterized by a CG-dominated microstructure. These differentiated microstructures can change the critical temperature T_A for the reverse transformation after unloading, by influencing $\Delta H^{M\text{-}A}$, $\Delta G_{mech}^{M\text{-}A}$, $\Delta E_{el}^{M\text{-}A}$, $\Delta E_{ir}^{M\text{-}A}$, and $\Delta S_{stress}^{M\text{-}A}$, thus further tailoring the corresponding functional behavior.

(4) A cascade architecture consisting of two groups of laser-additive-manufactured NiTi-based double-helix structures was built to verify the feasibility of the thermally driven elastocaloric cooling device. The results show that the refrigerant spring generated a ΔT_{ad} of 0.75 °C using the thermal actuator, which is marginally lower than that (1.07 °C) produced by the normal mechanical loading.

Declaration of competing interest

The authors declare that they have no known competing financial interests or personal relationships that could have influenced the work reported in this paper.

CRediT authorship contribution statement

Xiangbin Xu: Writing—original draft, Validation, Methodology, Investigation, Formal analysis, Data curation. **Chenglong Ma**: Writing—review & editing, Supervision, Project administration, Investigation, Funding acquisition, Conceptualization. **Rossitza Setchi**: Writing—review & editing, Supervision, Investigation. **Yu Liu**: Writing—review & editing, Formal analysis, Investigation. **Dongya Li**: Writing—review and editing, Methodology, Investigation. **Guotao Zhang**: Writing—review, editing, & investigation. **Quanlong Wang**: Writing—review & editing, Investigation. **Meiping Wu**: Writing—review & editing, Supervision, Investigation.

Acknowledgments

This work was supported by National Natural Science Foundation of China (Grant Nos. 52475358 and 52105345), Key Research and Development Plan of Jiangsu Province (Grant No. BE2022069-2), Jiangsu Province Youth Talent Support Program (Grant No. JSTJ-2024-450), and Postgraduate Research & Practice Innovation Program of Jiangsu Province (Grant No. SJCX25_1324).

Declaration of generative AI in scientific writing

Generative AI and AI-assisted technologies were not used in the writing process.

References

[1] Chen YL, Wang Y, Sun Wang, et al. A compact elastocaloric refrigerator. Innovation 2022;3(2):100205. https://doi.org/10.1016/j.xinn.2022.100205.

[2] Soori M, Arezoo B, Smart materials and alloys for additive manufacturing integration: A review. Chin J Mech Eng Addit Manuf Front 2025;4(4):200242. https://doi.org/10.1016/j.amf.2025.200242.

[3] Wang SY, Shi YJ, Li Y, et al. Solid-state refrigeration of shape memory alloy-based elastocaloric materials: A review focusing on preparation methods, properties and development. Renew Sust Energ Rev 2023;187:113762. https://doi.org/10.1016/j.rser.2023.113762.

[4] Peng X, Yuan LH, Dai DH, et al. Novel class of additive manufactured niti-based hierarchically graded chiral structure with low-force compressive actuation for elastocaloric heat pumps. Chin J Mech Eng Addit Manuf Front 2023;2:100077. https://doi.org/10.1016/j.cjmeam.2023.100077.

[5] Greco A, Aprea C, Maiorino A, et al. A review of the state of the art of solid-state caloric cooling processes at room-temperature before 2019. Int J Refrig 2019;106:66-88. https://doi.org/10.1016/j.ijrefrig.2019.06.034.

[6] Qian SX, Catalini D, Muehlbauer J, et al. High-performance multimode elastocaloric cooling system. Science 2023;380:722-727. https://doi.org/10.1126/science.adg7043.

[7] Wang K, Engelbrecht K, Bahl CRH, et al. Additive manufactured thermoplastic elastomers for low-stress driven elastocaloric cooling. Appl Mater Today 2023;20:101711. https://doi.org/10.1016/j.apmt.2022.101711.

[8] Qian SX, Wang Y, Yuan LF, et al. A heat driven elastocaloric cooling system. Energy 2019;182:881-899. https://doi.org/10.1016/j.energy.2019.06.094.

[9] Wang J, Huang B, Gu XJ, et al. Actuation performance of machined helical springs from NiTi shape memory alloy. Int J Mech Sci 2022;236:107744. https://doi.org/10.1016/j.ijmecsci.2022.107744.

[10] Wang Y, Liu Y, Xu SJ, et al. Towards practical elastocaloric cooling. Commun Eng 2023;2:79. https://doi.org/10.1038/s44172-023-00129-5.

[11] Yuan LF, Wang Y, Yu JL, et al. Numerical study of a double-effect elastocaloric cooling system powered by low-grade heat. Appl Therm Eng 2023;218:119302. https://doi.org/10.1016/j.applthermaleng.2022.119302.

[12] Frenzel J, George EP, Dlouhy A, et al. Influence of Ni on martensitic phase transformations in NiTi shape memory alloys. Acta Mater. 2010;58:3444-3458. https://doi.org/10.1016/j.actamat.2010.02.019.

[13] Wei SS, Zhang JL, Zhang L, et al. Laser powder bed fusion additive manufacturing of NiTi shape memory alloys: A review. Int. J Extreme Manuf 2023;5:032001. https://doi.org/10.1088/2631-7990/acc7d9.

[14] Kumar P, Suryavanshi P, Dwivedy SK, et al. Stimuli-responsive materials for 4D Printing: Mechanical, manufacturing, and biomedical applications. J. Mol. Liq. 2024;410:125553. https://doi.org/10.1016/j.molliq.2024.125553.

[15] Yan JX, Cai B, Ou BX, et al. Effect of laser energy density on the phase transformation behavior and functional properties of NiTi shape memory alloy by selective laser melting. J. Alloy. Compd. 2024;1005:176060. https://doi.org/10.1016/j.jallcom.2024.176060.

[16] Guo WQ, Sun Z, Yang Y, et al. Study on the junction zone of NiTi shape memory alloy produced by selective laser melting via a stripe scanning strategy. Intermetallics 2020;126:106947. https://doi.org/10.1016/j.intermet.2020.106947.

[17] Wang XB, Yu JY, Liu JW, et al. Effect of process parameters on the phase transformation behavior and tensile properties of NiTi shape memory alloys fabricated by selective laser melting. Addit Manuf 2020;36:101545. https://doi.org/10.1016/j.addma.2020.101545.

[18] Hou HL, Simsek E, Ma T, et al. Fatigue-resistant high-performance elastocaloric materials made by a

dditive manufacturing. Science 2019;366:1116-1121. https://doi.org/10.1126/science.aax7616.

[19] Peng X, Yuan LH, Dai DH, et al. Novel new class of additive manufactured NiTi-based hierarchically graded chiral structure with low-force compressive actuation for elastocaloric heat pumps. Chin J Mech Eng Addit Manuf Front 2023;2:100077. https://doi.org/10.1016/j.cjmeam.2023.100077.

[20] Kordizadeh F, Safaei K, Mohajerani S, et al. Investigation of the elastocaloric effect in laser powder bed fusion NiTi porous structures. Addit Manuf Lett 2023;6:100131. https://doi.org/10.1016/j.addlet.2023.100131.

[21] Cao YX, Zhou XL, Cong DY, et al. Large tunable elastocaloric effect in additively manufactured Ni-Ti shape memory alloys, Acta Mater. 194 (2020) 178-189. https://doi.org/10.1016/j.actamat.2020.04.007.

[22] Zhan JB, Li K, Ma RJ, et al. Achieving fine tailoring of elastocaloric properties of laser powder bed-fused NiTi alloy via laser beam manipulation. Int J Mach Tools Manuf 2024;202:104240. https://doi.org/10.1016/j.ijmachtools.2024.104210.

[23] Lu H, Liu L, Luo X, et al. Formation mechanism of heterogeneous microstructures and shape memory effect in NiTi shape memory alloy fabricated via laser powder bed fusion. Mater Des 2023;232:112107. https://doi.org/10.1016/j.matdes.2023.112107.

[24] Ma CL, Gu DD, Setchi R, et al. A large compressive recoverable strain induced by heterogeneous microstructure in a $Ni_{50.6}Ti_{49.4}$ shape memory alloy via laser powder bed fusion and subsequent aging treatment. J Alloy Compd 2022;918:165620. https://doi.org/10.1016/j.jallcom.2022.165620.

[25] Mari D, Dunand D. NiTi and niti-tic composites: Part 1. transformation and thermal cycling behavior. Metall Mater Trans A 1995;26:2833-2847. https://doi.org/10.1007/BF02669642.

[26] Lu SJ, Li Y, Zhen SY, et al. Influence of process parameters on the microstructures, residual stresses and mechanical properties of TA15 titanium alloy fabricated by L-PBF. Mater Sci Eng A-Struct Mater Prop Microstruct Process 2025;927:147990. https://doi.org/10.1016/j.msea.2025.147990.

[27] Tong HC, Wayman CM. Characteristic temperatures and other properties of thermoelastic martensites. N/A 1974;22:887-896. https://doi.org/10.1016/0001-6160(74)90055-8.

[28] Ding L, Zhou YM, Xu YY, et al. Learning from superelasticity data to search for Ti-Ni alloys with large elastocaloric effect. Acta Mater 2021;218:117200. https://doi.org/10.1016/j.actamat.2021.117200.

[29] Chen JY, Liu BQ, Xing LL, et al. Toward tunable mechanical behavior and enhanced elastocaloric effect in NiTi alloy by gradient structure. Acta Mater 2022;226:117609. https://doi.org/10.1016/j.actamat.2021.117609.

[30] Otsuka K, Ren X. Physical metallurgy of Ti-Ni-based shape memory alloys. Prog Mater Sci 2005;50

(5):511-678. https://doi.org/10.1016/j.pmatsci.2004.10.001.

[31] Ma H, Lu H, Kang L, et al. Enhanced thermal cycle stability and shape memory effect in NiTiHf shape memory alloys fabricated by laser powder bed fusion. Addit Manuf 2024;92:104375. https://doi.org/10.1016/j.addma.2024.104375.

[32] Atli KC, Karaman I, Noebe RD, et al. The effect of training on two-way shape memory effect of binary NiTi and NiTi based ternary high temperature shape memory alloys. Mater Sci Eng A-Struct Mater Prop Microstruct Process 2013;560:653-666. https://doi.org/10.1016/j.msea.2012.10.009.

[33] Ponikarova I, Resnina N, Belyaev S, et al. Influence of maximum thermal cycle temperature on the two-way shape memory effect in TiNi Alloy. Mater Today Proc 2017;4:4734-4742. https://doi.org/10.1016/j.matpr.2017.04.062.

[34] Yu QJ, Liu Y, Si C, et al. Incommensurate modulated structure and its influence on the martensitic transformation temperature span of single phase multielement Ni-Cu-Co-Mn-Ga two-way shape memory single crystals. J Mater Sci Technol 2025;208:230-240. https://doi.org/10.1016/j.jmst.2024.04.069.

[35] Balak Z, Abbasi S. Influence of the Ti content, training cycles and pre-strain on the two-way shape memory effect in NiTi alloys. Mater Des 2011;32(7):3992-3996. https://doi.org/10.1016/j.matdes.2011.03.036.

[36] Ma CL, Wu MP, Dai DH, et al. Stress-induced heterogeneous transformation and recoverable behavior of laser powder bed fused Ni-rich $Ni_{50.6}Ti_{49.4}$ alloys without post treatment. J Alloy Compd 2022;905:164212. https://doi.org/10.1016/j.jallcom.2022.164212.

[37] Zhang H, Dai DH, Yuan LH, et al. Temperature gradient induced tough-brittle transition behavior of a high-strength Al-4.2Mg-0.4Sc-0.2Zr alloy fabricated by laser powder bed fusion additive manufacturing. Addit Manuf 2023;73:103655. https://doi.org/10.1016/j.addma.2023.103655.

[38] Zhuo Z, Fang ZY, Ma CL, et al. Influence of LaB6 inoculant on the thermodynamics within the molten pool and subsequent microstructure development and cracking behavior of laser powder bed fused TiAl-based alloys. J Mater Res Technol-JMRT 2023;27:2363-2381. https://doi.org/10.1016/j.jmrt.2023.10.062.

[39] DebRoy T, Wei HL, Zuback JS, et al. Additive manufacturing of metallic components-Process, structure and properties. Prog Mater Sci 2018;92:112-224. https://doi.org/10.1016/j.pmatsci.2017.10.001.

[40] Gu DD, Ma CL, Dai DD, et al. Additively manufacturing-enabled hierarchical NiTi-based shape memory alloys with high strength and toughness. Virtual Phys Prototyp 2021;16:S19-S38. https://doi.org/10.1080/17452759.2021.1892389.

[41] Chen JA, Liu ZZ, Liu C, et al. Effects of scanning strategy and scanning speed on microstructures a

nd mechanical properties of NiTi alloys by laser powder bed fusion. Mater Sci Eng A-Struct Mater Prop Microstruct Process 2024;914:147115. https://doi.org/10.1016/j.msea.2024.147115.

[42] McCormick PG, Liu Y. Thermodynamic analysis of the martensitic transformation in NiTi-II. Effect of transformation cycling. Acta Metall Mater 1994;42:2407-2413. https://doi.org/10.1016/0956-7151(94)90319-0.

[43] Prokoshkin SD, Korotitskiy AV, Brailovski V, et al. On the lattice parameters of phases in binary Ti-Ni shape memory alloys. Acta Mater 2004;52(15):4479-4492. https://doi.org/10.1016/j.actamat.2004.06.007.

[44] Niitsu K, Kimura Y, Xu X, et al. Composition dependences of entropy change and transformation temperatures in Ni-rich Ti-Ni system. Shape Mem Superelasticity. 2015;1:124-131. https://doi.org/10.1007/s40830-015-0023-2.

[45] Zhou N, Shen C, Wagner MFX, et al. Effect of Ni_4Ti_3 precipitation on martensitic transformation in Ti-Ni. Acta Mater 2010;58(20):6685-6694. https://doi.org/10.1016/j.actamat.2010.08.033.

[46] Tyc O, Bian X, Molnárová O, et al. Martensitic transformation induced by cooling NiTi wire under various tensile stresses: Martensite variant microstructures, textures, recoverable strains and plastic strains. Appl Mater Today 2024;41:102448. https://doi.org/10.1016/j.apmt.2024.102448.

[47] Qie X, Li YJ, Lin JP. Grain size-dependent martensitic transformation and localized plastic deformation mechanism in NiTi alloys at mesoscopic scale. Mater Sci Eng A-Struct. Mater Prop Microstruct Process 2025;945:148986. https://doi.org/10.1016/j.msea.2025.148986

[48] Ahadi A, Sun QP. Stress hysteresis and temperature dependence of phase transition stress in nanostructured NiTi-Effects of grain size. Appl Phys Lett 2013;103(2):021902. https://doi.org/10.1063/1.4812643.

[49] Liu JY, DengYL, Guo XB. Study the correlation of B19' phase transformation and grain orientation evolution on shape recovery of NiTi alloys fabricated by powder bed fusion. Mater Charact 2023;205:113297. https://doi.org/10.1016/j.matchar.2023.113297.

[50] Matsumoto O, Miyazaki S, Otsuka K, et al. Crystallography of martensitic transformation in TiNi single crystals. N/A 1987;35:2137-2144. https://doi.org/10.1016/0001-6160(87)90042-3.

[51] Peng X, Ma CL, Yuan LH, et al. Understanding the role of laser processing parameters and position-dependent heterogeneous elastocaloric effect in laser powder bed fused NiTi thin-walled structures. Smart Mater Struct 2024;33(4):045003. https://doi.org/10.1088/1361-665X/ad2c6c.

[52] Wang SY, Shi YJ, Fan KJ, et al. Role of process parameters on the elastocaloric effect of thin-walled NiTi shape memory alloys fabricated by additive manufacturing at the same energy density. J Manuf Process 2025;149:345-363. https://doi.org/10.1016/j.jmapro.2025.05.074.

[53] Wang SY, Shi YJ, Fan KJ, et al. Microstructure and elastocaloric effect of NiTi shape memory alloy in-situ synthesized by laser directed energy deposition additive manufacturing. Mater Charact 2024;210:113831. https://doi.org/10.1016/j.matchar.2024.113831.

[54] Wang SY, Shi YJ, Zhao XJ, et al. Tailoring microstructure and strengthening mechanism of anisotropic elastocaloric effect in NiTi shape memory alloys by laser directed energy deposition scanning strategy J Mater Process Technol 2025;339:118825. https://doi.org/10.1016/j.jmatprotec.2025.118825.

[55] Li SS, Guo WQ, Ran XZ, et al. Microstructure evolution and elastocaloric properties of in-situ metallurgical NiTi alloys in a wide composition range by laser additive manufacturing technology. J Alloy Compd 2025;1021:179698. https://doi.org/10.1016/j.jallcom.2025.179698.

[56] Liu Y, Xie CX, Zhang C, et al. Microstructure and elastocaloric properties of in-situ NiTiFe alloys prepared via laser engineered net shaping. Mater Sci Eng A-Struct Mater Prop Microstruct Process 2025;945:148972. https://doi.org/10.1016/j.msea.2025.148972.

[57] Zhang MG, Fang XW, Li XZ, et al. Tailorable elastocaloric cooling performance of wire-arc directed energy deposition NiTi alloy through concentration gradient design. J Mater Sci Technol 2025;226:229-244. https://doi.org/10.1016/j.jmst.2024.11.058.

[58] Kordizadeh F, Mohajerani S, Safaei K, et al. Investigating the elastocaloric effect of the NiTi fabricated by laser powder bed fusion: Effect of the building orientation. Materialia 2023;30:101817. https://doi.org/10.1016/j.mtla.2023.101817.

[59] Kim HC, Yoo YI, Lee JJ. Development of a NiTi actuator using a two-way shape memory effect induced by compressive loading cycles. Sens Actuator A-Phys 2008;148(2):437-442. https://doi.org/10.1016/j.sna.2008.08.019.

[60] Resnina N, Belyaev S, Voronkov A, et al. Shape memory effects in porous Ti-45.0 at.% Ni alloy produced by self-propagating high-temperature synthesis. Mater Today Proc 2017;4:4690-4695. https://doi.org/10.1016/j.matpr.2017.04.053.

[61] Falvo A, Furgiuele FM, Maletta C, et al. Functional behaviour of a NiTi-welded joint: Two-way shape memory effect. Mater Sci. Eng A-Struct Mater Prop Microstruct Process 2008;481:647-650. https://doi.org/10.1016/j.msea.2006.11.178.

[62] Kireeva IV, Pobedennaya ZV, Chumlyakov YI, et al. Superelasticity and two-way shape memory effect in 001 -oriented TiNiCu single crystals under compression. Mater Lett 2020;281:128646. https://doi.org/10.1016/j.matlet.2020.128646.

[63] Chen YX, Li A, Ma ZY, et al. Step-wise R phase transformation rendering high-stability two-way sh

ape memory effect of a NiTiFe-Nb nanowire composite. Acta Mater 2021;219:117258. https://doi.org/10.1016/j.actamat.2021.117258.

[64] Meng XL, Zheng YF, Cai W,et al. Two-way shape memory effect of a TiNiHf high temperature shape memory alloy. J Alloy Compd 2004;372(1-2):180-186. https://doi.org/10.1016/j.jallcom.2003.10.020.

[65] Resnina N, Belyaev S, SlesarenkoV, et al. Influence of crystalline phase volume fraction on the two-way shape memory effect in amorphous-crystalline $Ti_{40.7}Hf_{9.5}Ni_{44.8}Cu_5$ alloy. Mater Sci Eng A-Struct Mater Prop Microstruct Process 2015;627:65-71. https://doi.org/10.1016/j.msea.2014.12.119.

[66] Zhou XJ, Huang ZH, Chen F, et al. Two-way shape memory effect with excellent cycling stability in TiNiCuNb alloy. Mater Lett 2022;308:131256. https://doi.org/10.1016/j.matlet.2021.131256.

Declaration of interests

☒ The authors declare that they have no known competing financial interests or personal relationships that could have appeared to influence the work reported in this paper.